ELSEVIER

Contents lists available at ScienceDirect

# Geochimica et Cosmochimica Acta

journal homepage: www.elsevier.com/locate/gca





# Iron isotope fractionation during partial melting of metapelites and the generation of strongly peraluminous granites

Juan David Hernández-Montenegro <sup>a,\*</sup>, Claire E. Bucholz <sup>a</sup>, Emma S. Sosa <sup>a</sup>, Michael A. Kipp <sup>b,1</sup>, François L.H. Tissot <sup>b</sup>

- <sup>a</sup> Division of Geological and Planetary Sciences, California Institute of Technology, Pasadena, CA, USA
- <sup>b</sup> The Isotoparium, Division of Geological and Planetary Sciences, California Institute of Technology, Pasadena, CA, USA

#### ARTICLE INFO

Associate editor: Stefan Weyer

Keywords:
Fe isotopes
Strongly peraluminous granite (SPG)
Phase equilibria
Partial melting
Isotopic fractionation

#### ABSTRACT

The large variability in Fe isotope ratios of sedimentary rocks (particularly those from the Archean and Proterozoic) contrasts with that of igneous rocks, which display a much more limited range in values. Notably, among igneous rocks, those inferred to form via partial melting of siliciclastic sediments – strongly peraluminous granites (SPGs) – exhibit greater variability in their Fe isotope compositions, suggesting SPGs may capture isotopic variations in the sedimentary record. However, the extent and mechanisms of iron isotope fractionation between SPGs and their source remain poorly understood. Our study integrates iron isotope analyses with petrological modeling to investigate equilibrium isotopic fractionation during generation of SPG magmas. As a case study, we focus on the Neoarchean Ghost Lake Batholith and the adjacent metasedimentary rocks in Ontario, Canada. These units represent an internally differentiated SPG batholith and metamorphosed sedimentary rocks interpreted as the source of the batholith.

We measured  $\delta^{56}$ Fe compositions of SPG samples, metasedimentary rocks, and a restitic rock. Sulfide grains were also measured in four metapelite samples and a granite sample. We find no correlation between the  $\delta^{56}$ Fe composition of metasedimentary rocks and their metamorphic grade, indicating iron isotopes behave as a closed system during metamorphism. Modeling results show that iron isotopes in SPGs from the Ghost Lake batholith are consistent with equilibrium fractionation during biotite dehydration melting, with predicted  $\delta^{56}$ Fe values for melts and restitic assemblages mainly controlled by the source composition. Our results predict negligible isotopic fractionation between the residue and the source, whereas  $\sim 0.177-0.277$  % is expected between SPG melts and the residue, accounting for high  $\delta^{56}$ Fe values in granite samples. Lower  $\delta^{56}$ Fe values may indicate that some granites represent mixtures of melt and cumulus material or result from assimilation of restite or source/host rock. However, despite deviations from pure equilibrium fractionation, the variability in  $\delta^{56}$ Fe values for SPGs is about one order of magnitude smaller than that seen in the sedimentary record for the Archean and Proterozoic ( $\sim 0.2$  % vs. > 2 %). We posit that this narrower range of isotopic variation in SPGs results from metamorphism and partial melting, which can homogenize large isotopic variations in sedimentary protoliths. Thus, SPGs represent reliable archives for the bulk iron isotope evolution of siliciclastic sedimentary rocks through time.

# 1. Introduction

Numerous studies have examined iron isotopes in sedimentary rocks to probe variations in the marine Fe cycle due to the sensitivity of this system to variations in dissolved  $O_2$  and S concentrations (e.g., Johnson et al., 2003, 2008; Matthews et al., 2004; Rouxel et al., 2005; Yamaguchi et al., 2005; Hofmann et al., 2009; Bekker et al., 2010; Planavsky et al.,

2012; Busigny et al., 2014; Marin-Carbonne et al., 2014, 2020; Yoshiya et al., 2015b; Heard et al., 2020; Ostrander et al., 2022; Dupeyron et al., 2023). Variability of several permil in  $\delta^{56} Fe$  (where  $\delta^i Fe_{unknown} = \left[ ({}^i Fe/^{54} Fe)_{unknown}/({}^i Fe/^{54} Fe)_{standard} -1 \right] \times 10^3)$  has been documented in bulk-rock analyses and mineral separates (e.g., Rouxel et al., 2005; Dauphas et al., 2017; Heard and Dauphas, 2020; Ostrander et al., 2022; Dupeyron et al., 2023; Fig. 1a). In particular, temporal

<sup>\*</sup> Corresponding author.

E-mail address: jdhernandez@caltech.edu (J.D. Hernández-Montenegro).

Now at Division of Earth and Climate Sciences, Duke University, Durham, North Carolina, USA.

trends in iron isotope ratios of sedimentary rocks and pyrites have been widely interpreted to reflect the evolution of the global oceanic Fe cycle and its relationship to changes in atmospheric oxygenation through time (Beard and Johnson, 2004; Dauphas et al., 2004, 2017; Johnson et al., 2004; Rouxel et al., 2005; Anbar and Rouxel, 2007; Planavsky et al., 2012; Busigny et al., 2014; Ostrander et al., 2022; Dupeyron et al., 2023).

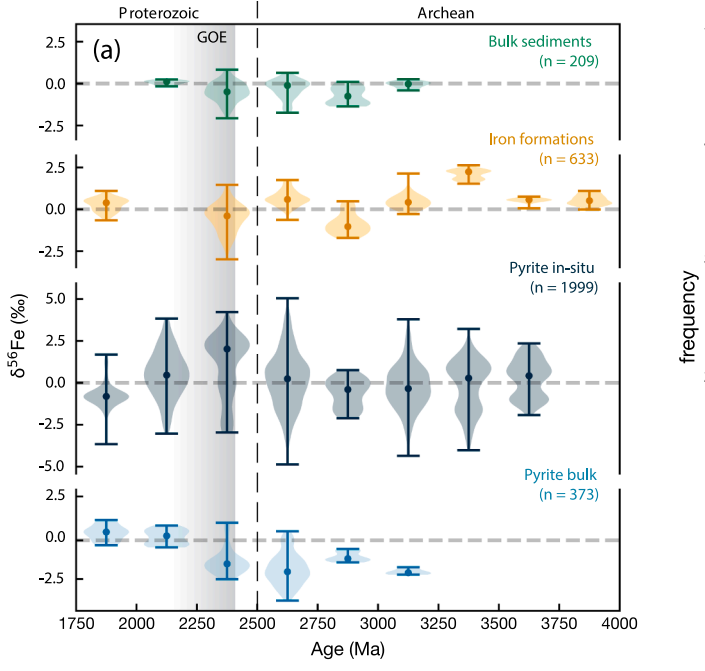
One complexity that arises in interpreting Fe isotope compositions from sedimentary rocks is comparing data from different scales of analysis (i.e., bulk-rock, bulk-mineral, or in-situ mineral). For example, most studies have focused on bulk-rock  $\delta^{56}$ Fe compositions (e.g., Matthews et al., 2004; Yamaguchi et al., 2005; Johnson et al., 2008; Fabre et al., 2011; Busigny et al., 2014; Heard et al., 2020; Ostrander et al., 2022) or bulk mm-scale pyrite grains extracted from their matrix in sedimentary rocks (e.g., Rouxel et al., 2005; Archer and Vance, 2006; Hofmann et al., 2009). Recognizing that this latter approach can introduce sampling bias towards visible pyrite grains, other studies have conducted in-situ analyses of pyrites at the micron scale (e.g., Yoshiya et al., 2012, 2015a, 2015b; Marin-Carbonne et al., 2014, 2020; Agangi et al., 2015; Dupeyron et al., 2023). These latter studies have demonstrated large and constant ranges of  $\delta^{56}$ Fe values in pyrite, ranging from around -4 to +4 % through geologic time (Dupeyron et al., 2023; Fig. 1a). Thus, the scale of isotopic variability in sedimentary rocks may be on the inter- or even intra-mineral scale and analyses of mineral separates or in-situ analyses will not necessarily be representative of bulk-rock compositions.

Furthermore, bulk-rock samples from individual Precambrian sedimentary formations can have  $\delta^{56}$ Fe values that vary by >1 ‰ (e.g., Yamaguchi et al., 2005; Johnson et al., 2008; Bekker et al., 2010; Fabre et al., 2011; Busigny et al., 2014; Heard et al., 2020; Ostrander et al.,

2022), reflecting the relative proportions of isotopically distinct mineral components. Detrital and authigenic silicates, which typically dominate siliciclastic rocks, are expected to have  $\delta^{56} \text{Fe}$  values averaging zero, similar to that of near-modern loess, river loads, and marine sediments, as well as the average of igneous rocks (Beard and Johnson, 2004; Yamaguchi et al., 2005; Dauphas et al., 2017; Slotznick et al., 2018; Fig. 1b). In contrast, sulfide-rich rocks can have highly variable iron isotope compositions. For example, Archean bulk sediments, largely influenced by pyrite-rich black shales, display prominent excursions toward negative  $\delta^{56} \text{Fe}$  values (Rouxel et al., 2005; Yamaguchi et al., 2005; Ostrander et al., 2022; Dupeyron et al., 2023; Fig. 1a).

Given the inherent variability and complexities of the sedimentary iron isotope record, this work focuses on strongly peraluminous granites (SPGs), derived from partial melting of siliciclastic sediments. SPGs are defined by their bulk-rock chemistry, with aluminum saturation values (ASI = molar  $Al_2O_3/[CaO + Na_2O + K_2O]$ ) greater than 1.1, and are often informally referred to as "S-types" (Chappell and White, 1992; Clarke, 2019; Nabelek, 2020; Bucholz, 2024). Because SPGs homogenize their sedimentary source material, they may represent a complementary archive to siliciclastic rocks, potentially recording significant changes in global cycles and geological processes throughout Earth's history (e.g., Bucholz and Spencer, 2019; Bucholz et al., 2020; Liebmann et al., 2021; Bucholz, 2022). It is important to note, however, that unlike chemical sediments, which may reflect changes in ocean chemistry over time, the iron isotope composition of SPGs will also be influenced by the composition of detrital sediments sourced from proximal continental settings.

Before being able to potentially use SPGs to track changes in the bulk Fe isotopic composition of sedimentary rocks, it is critical to understand whether metamorphism and partial melting of metasedimentary rocks



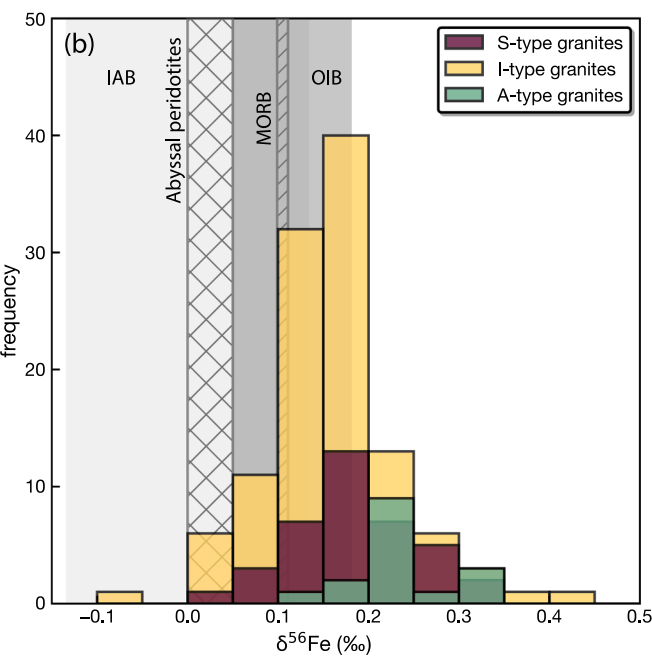


Fig. 1. Iron isotope compositions of the main sedimentary reservoirs (a) and different types of igneous rocks (b). a) Violin plots show compiled data of iron isotope compositions for bulk sediments (green), iron formations (yellow), and pyrite grains (in-situ: dark blue; bulk: dark light blue) in time-bins of 250 Ma. Most data for iron formations and pyrite comes from previous compilations by Heard and Dauphas (2019) and Dupeyron et al. (2023), updated with additional measurements from Fabre et al. (2011), Heard et al. (2020), and Ostrander et al. (2022). Bulk sediments include measurements of shales and greywackes from Yamaguchi et al. (2005), Heard et al. (2020), and Ostrander et al. (2022) b) Proterozoic to Phanerozoic granites (sensu lato:  $SiO_2 > 66$ %; S-type (red) I-type (yellow), and A-type (green) reach higher  $\delta^{56}$ Fe values than more mafic rocks (Poitrasson and Freydier, 2005; Heimann et al., 2008; Telus et al., 2012; Sossi et al., 2012; Foden et al., 2015, 2018; He et al., 2017; Liang et al., 2022; Liou et al., 2022; Ma et al., 2022; Zhang et al., 2023). Abyssal peridotites, representative of the mantle of mid-ocean ridge basalts (MORB), have  $\delta^{56}$ Fe of 0.025 %  $\pm$  0.025 % (Craddock et al., 2013), whereas MORBs display a more homogeneous composition of 0.105 %  $\pm$  0.006 % (Teng et al., 2013). Ocean island basalts (OIB) have  $\delta^{56}$ Fe ranging from 0.05 to 0.18 % (Teng et al., 2013), and island arc basalts (IAB) vary between -0.133 and 0.133 % (Sossi et al., 2016

fractionate iron isotopes and, if so, to what extent? Here, we investigate the fractionation of iron isotopes during partial melting of metasedimentary rocks and how this process is imprinted in the isotopic signature of SPGs through analysis of natural samples capturing this process and associated modeling. First, we measured the iron isotope composition of the SPGs from the Neoarchean Ghost Lake batholith (GLB) in Ontario, Canada, and associated metasedimentary rocks from the Zealand unit, thought to be representative of its source. We then used thermodynamic phase equilibrium modeling to assess the extent of equilibrium isotopic fractionation during partial melting of the metasedimentary source and production of SPGs and compare this to our data. We discuss the influence of various factors, such as the source rock, fO<sub>2</sub>, P–T conditions, mineral composition changes, and the melt fraction, on the isotopic composition of the melts from which the GLB crystallized and assess whether SPGs faithfully record the iron isotope composition of their metasedimentary source rocks.

# 2. Fe isotopes during metamorphism and generation of SPG magmas

Currently, there are only limited SPG Fe isotope data, comprising a broad survey of Paleozoic SPGs mainly from Australia and Tasmania (n = 15; Foden et al., 2015), as well as a more focused study on migmatites (n = 11; six leucosomes and five melanosomes) and granites (n = 11)from the Paleoproterozoic Harney Peak granite in South Dakota (Telus et al., 2012). SPGs (and granites in general) have heavy and variable iron isotope compositions compared to more mafic igneous rocks, with  $\delta^{56}$ Fe in SPGs up to +0.32 % (Telus et al., 2012; Foden et al., 2015; Dauphas et al., 2017; Bucholz, 2024; Fig. 1b). Several mechanisms have been proposed to explain the heavy isotopic composition of granites; however, most studies point to equilibrium fractionation during fractional crystallization or partial melting, producing isotopically light cumulates or restites and heavy granitic melts (e.g., Schuessler et al., 2009; Telus et al., 2012; Sossi et al., 2012; Foden et al., 2015, 2018). Dauphas et al. (2014) found that the mean force constants for iron in silicate glasses increased with higher  $SiO_2$  contents and  $Fe^{3+}/\Sigma Fe$  ratios (i.e,  $Fe^{3+}/(Fe^{3+} + Fe^{2+})$ ). These relationships imply that the magnitude of isotopic fractionation in silicate melts also increases as melts become more SiO2-rich, reflecting changes in the average coordination of iron with higher degrees of polymerization. Thus, highly differentiated melts, such as those from fractional crystallization or low degrees of partial melting, should be isotopically heavier than less polymerized melts at a given oxidation state.

When considering SPGs specifically, however, if and how metamorphism and anatexis of metasedimentary rocks fractionate iron isotopes have yet to be thoroughly explored. The effects of metamorphism prior to anatexis have received more attention since most Precambrian sedimentary rocks have experienced some metamorphism (Marin-Carbonne et al., 2020; Dupeyron et al., 2023), which may affect the associated iron isotope record. In general, it is expected that, as temperature increases, variability in  $\delta^{56}$ Fe between minerals will diminish (Dauphas et al., 2007a, 2007b). Frost et al. (2007) and Hyslop et al. (2008), for example, showed that at low metamorphic grades, banded iron formations preserve large inter-mineral isotopic variations, but at higher grades, isotopic ratios are homogenized. However, complete isotopic reequilibration may not occur for all minerals during metamorphism. Studies focusing on pyrite across various metamorphic grades, for example, reveal persistent intra-sample variability in  $\delta^{56}$ Fe values from prehnite-pumpellyite to amphibolite facies (Whitehouse and Fedo, 2007; Galić et al., 2017; Marin-Carbonne et al., 2020; Dupeyron et al., 2023). Regardless of whether inter-mineral homogenization occurs or not, metamorphism of sedimentary rocks can generally be considered a near-closed system process, at least in terms of Fe isotopes, where the isotopic composition of the protolith is preserved by bulk rocks (e.g., Frost et al., 2007; Dauphas et al., 2007a, b; Hyslop et al., 2008; Marin-Carbonne et al., 2020; Dupeyron et al., 2023). This means that prograde metamorphism should preserve the bulk isotopic composition of the protolith, even if original isotopic variations are erased due to isotopic homogenization or mineral transformations occurring during metamorphism.

Significant isotopic fractionation may, however, occur between the melt and the residual sedimentary source upon crossing the solidus. Production of SPG magmas dominantly occurs via dehydration reactions that produce melt and residual minerals with varying compositions as melting progresses (Thompson, 1982; Le Breton and Thompson, 1988; Patiño Douce and Beard, 1995; Patiño Douce and Harris, 1998; Sylvester, 1998; Spear et al., 1999). Telus et al. (2012) used the Harney Peak granite migmatites as a natural experiment to investigate this process. They measured five leucosome-melanosome pairs and two samples each of the Harney Peak granite and host-rock schists. They found that the  $\delta^{56}$ Fe of the leucosomes, representative of migmatite partial melts, were elevated by 0.05-0.20 % compared to their melanosome pairs, suggesting an equivalent magnitude of fractionation between partial melt and residue during anatexis. The  $\delta^{56}\mbox{Fe}$  values of the leucosomes (+0.246 to +0.480 %) were higher by 0-0.2 % than that of the two analyzed Harney Peak granite samples ( $+0.161 \pm 0.052$  % and  $+0.240 \pm 0.041$  %). No other study of natural samples representing the partial melting process of metasedimentary rocks has been undertaken. However, Xu et al. (2017) measured the iron isotope composition of migmatitic rocks from the Dabie orogen, China, likely derived from a dioritic to granodioritic protolith (Wang et al., 2013). The observed iron isotope fractionation between leucosomes and melanosomes from these rocks ranges  $\sim 0-0.36$  %, with leucosomes displaying higher  $\delta^{56}$ Fe values than melanosomes. Their results suggest significant equilibrium isotopic fractionation produced during partial melting, controlled mainly by differences in the iron bonding environment in granitic anatectic melts and complementary restites.

The extent of equilibrium isotopic fractionation during partial melting of metasedimentary rocks and generation of SPGs can be calculated using melting reactions and iron force constants for ironbearing phases relevant to the generation of magmas via high-grade metamorphism and partial melting (e.g., Dauphas et al., 2014; Nie et al., 2021; Polyakov et al., 2007; Roskosz et al., 2022, 2015). Such phases include silicate melts, biotite (annite), garnet (almandine), spinel (aluminum-bearing and magnetite), ilmenite, and orthopyroxene. Nie et al. (2021) produced a simplified model of biotite dehydration melting where 75 % of the iron produced via biotite breakdown entered garnet and the remaining 25 % entered the melt. They estimated the  $\delta^{56}$ Fe of the produced melt to be 0.2–0.3 % higher than the residue, in agreement with the empirical study of Telus et al. (2012). Anatexis is, however, a complex process where mass transfer is controlled by metamorphic reactions driven by changes in the equilibrium state of the system. Thus, more complex models incorporating changes in phase stability and composition along metamorphic paths are needed to capture iron isotope fractionation during partial melting more accurately. For example, the modal abundances of a phase, the amount of iron hosted in it, and the iron oxidation state are a function of the pressure (P), temperature (T), water content, and oxygen fugacity  $(fO_2)$  of the system, and all these variables influence the magnitude of iron isotope fractionation between minerals and melt.

To address the complexities of metamorphism and partial melting, we use a modeling approach that couples iron force constants with predicted stable phase assemblages under specific P-T- $fO_2$  conditions. This method effectively accounts for isotopic fractionation along a given metamorphic path, where continuous changes in phase compositions and proportions influence the iron bonding environment. In this study, we specifically apply this model to Fe isotopic fractionation between SPG magmas from the Ghost Lake batholith and its adjacent metasedimentary rocks, interpreted as the source of the batholith. We use this site as an ideal natural example where both SPGs and their protolith are preserved, allowing us to validate the model against actual Fe isotope measurements. However, while the results presented herein are

particular to the Ghost Lake batholith, the findings have broader implications for other SPGs across the geological record.

# 3. Regional geology

The Ghost Lake batholith and Zealand unit are part of the Sioux Lookout terrane in the Superior Province, Canada (Fig. 2), which lies at the boundary between granitic rocks of the Winnipeg River subprovince to the north and metavolcanic rocks from the Wabigoon subprovince to the south (Blackburn et al., 1991; Breaks and Moore, 1992). The sedimentary protoliths of the Zealand unit were turbiditic greywackes and mudstones and minor banded iron formations deposited ~2730-2700 Ma in an arc-proximal basin (Davis et al., 1988; Breaks and Moore, 1992). These sediments were later metamorphosed during the collision of the Wabigoon and Winnipeg River subprovinces, resulting in extensive melt production that produced the GLB (Breaks and Moore, 1992), which has a crystallization age obtained via U-Pb zircon geochronology at 2654  $\pm$  24 Ma (Liebmann et al., 2021). Peak metamorphic conditions have been estimated to reach  $\sim$ 0.3–0.4 GPa and  $\sim$ 550–750 °C (Breaks and Moore, 1992; Bucholz et al., 2020); however, rocks in the Zealand unit include a range of metamorphic facies, ranging from greenschist to upper-amphibolite facies with zones of incipient migmatization. Specifically, at the contact between the Zealand unit and the Wabigoon subprovince, the metamorphic grade is defined by the biotite-chlorite isograd, and it progressively increases to the north through the isograds of andalusite, garnet, sillimanite, and sillimanite-K-feldspar proximal to the GLB (Breaks and Moore, 1992). Migmatization and incipient partial melting of the Zealand unit are common at the west and northwest contacts with the GLB but absent at the east and south of the batholith (Bucholz et al., 2020).

Variability in mineral abundance and igneous textures defines eight subunits within the GLB (Breaks and Moore, 1992; Bucholz et al., 2020). The largest subunit, GLB-1, is a biotite and biotite-cordierite granite containing two elongated zones with abundant enclaves, identical to high-grade metamorphic rocks of the Zealand unit. GLB-2 is located at the western part of GLB-1, close to the contact with partially melted metasedimentary rocks from the Zealand unit. It consists of distinctive fine-grained, weakly deformed biotite granite dikes. GLB-3 is a  $\sim\!25\times2$ 

km strip along the southern contact of the GLB with the Zealand unit. This subunit consists of fine-grained biotite and muscovite granite with occasional accessory garnet and sillimanite. Segregations of leucogranite and K-feldspar-bearing pegmatites are ubiquitous within GLB-3. Finally, GLB-4 to -8 are restricted to the eastern portion of the GLB. These subunits form a complex of pegmatitic tourmaline + muscovite granites that lack metasedimentary enclaves. Overall, the western and central parts of the GLB are weakly deformed, with foliation decreasing toward the east, where the batholith appears more massive and commonly preserves magmatic foliation. A detailed study of the geology and geochemistry of the units that compose the GLB is provided in Breaks and Moore (1992).

#### 4. Methods

#### 4.1. Sample preparation

Granites (n=11), metasedimentary rocks from all metamorphic grades (n=11), and one restite from the GLB and Zealand unit were selected for whole-rock major and trace element chemistry and Fe isotope measurements. The initial sampled material consisted of several rock fragments (3–10 per sample), each weighing  $\sim$ 1–5 kg, collected *insitu*. Notably, for coarse-grained granite and pegmatite samples, either a greater number or larger volume of fragments were collected to account for their larger grain sizes. Rock powders for some of the samples studied here (n=9) were prepared for X-ray fluorescence (XRF) analysis and reported in previous studies (*i.e.*, Bucholz and Spencer, 2019; Bucholz et al., 2020). These powders were reused for Fe isotope measurements, and the whole-rock compositional data was taken from the original study (given in Supplementary Table S1). We prepared the remaining samples for which powders and XRF analyses were unavailable, following the procedure described below.

Only homogeneous rocks free of significant alteration or contamination were selected for Fe isotope analysis. Using a rock saw with a diamond blade, the samples were trimmed into cm-scale pieces to remove any altered surfaces. The cut rock pieces were then sanded to remove saw marks and sonicated in deionized water. After drying, samples were broken into  $1-2\,\mathrm{cm}$  pieces with a rock hammer and further

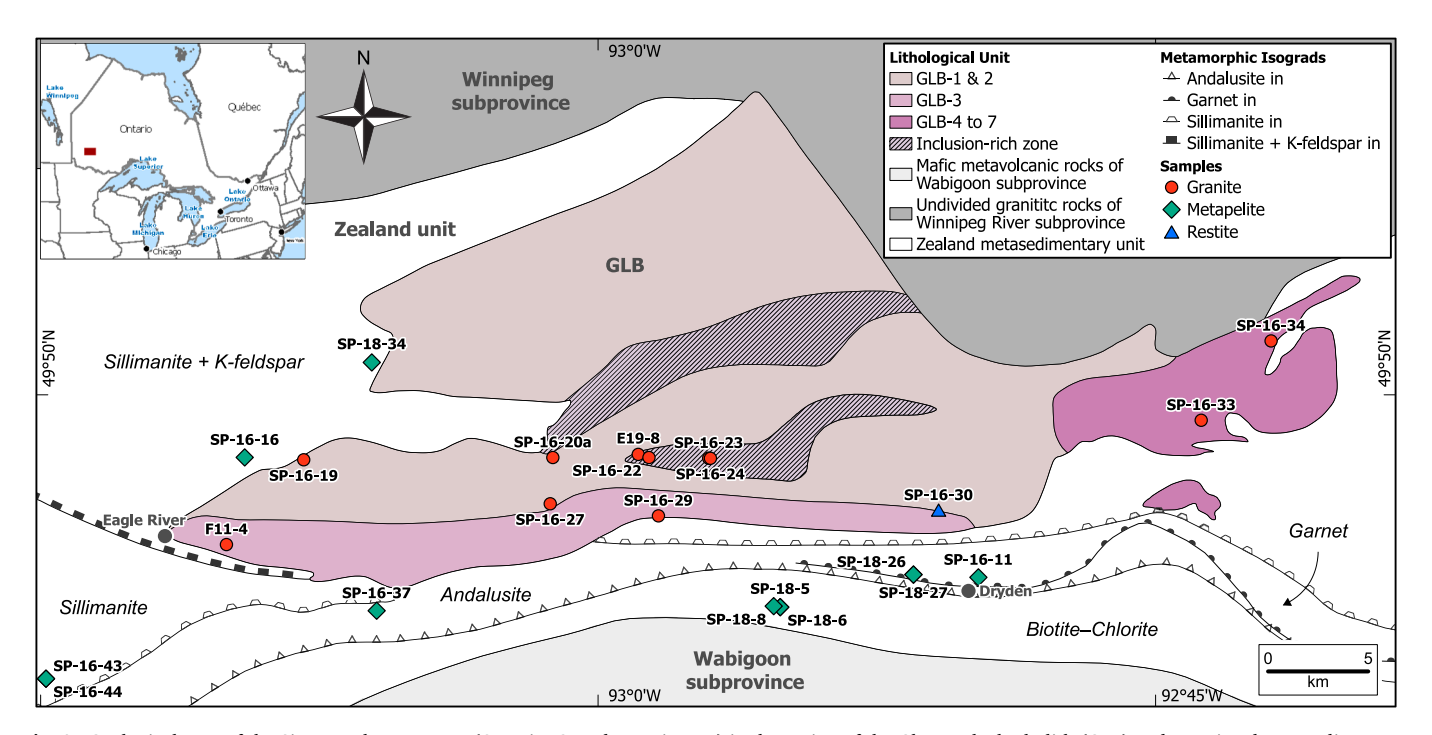


Fig. 2. Geological map of the Sioux Lookout terrane (Ontario, Canada, see inset a) in the region of the Ghost Lake batholith (GLB) and associated metasedimentary rocks corresponding to the Zealand unit (b). The map is modified from Breaks and Moore (1992) and Bucholz et al. (2020).

reduced to a grain size of 2–3 mm using a jaw crusher. Aliquots of  $\sim\!50{-}100$  g were typically taken from each sample. However, for coarse-grained granite and pegmatite samples, larger aliquots of  $\sim\!200$  g were collected to ensure representative sampling. Finally, after thorough homogenization, smaller aliquots of  $\sim\!40$  g were powdered in an agate grinding vessel with a ball mill.

Pyrrhotite grains were also separated from some samples to assess the effect of sulfides on the Fe isotopic composition of bulk-rock metapelites and granite samples. About 100–200 g sample powder was obtained by crushing cm-scale chips in an agate mortar. A pool of weakly magnetic grains was separated from the powder, and sulfide grains were manually picked under the microscope. 3–8 grains per sample with sizes  $<\!500~\mu m$  were then sonicated in DI water for five minutes to remove minute particles attached to them.

#### 4.2. Whole-rock and trace-element analysis

The major element composition of granites and metasedimentary rocks was determined by XRF analysis at Caltech. Powdered samples were dried at 110 °C overnight, and loss on ignition (LOI) was determined by sintering the dried powders for one hour at 1050 °C. The sintered powders were then homogenized with an agate mortar and pestle and fused into glass discs using platinum crucibles and molds. The glass discs were analyzed for major elements using a Panalytical Zetium 4 kW XRF spectrometer using the same analytical conditions described in Bucholz and Spencer (2019). After XRF analyses, chips of the glass discs were digested in acid and analyzed for trace element concentrations via inductively coupled mass spectrometry (ICPMS), also at Caltech (Lewis et al., 2021).

# 4.3. Fe isotope measurements

Whole-rock Fe isotope measurements were performed at the Isotoparium (Caltech) following the methods of Dauphas et al. (2004, 2009). Between 5 and 20 mg of sample powder was transferred to acid cleaned Teflon (PFA) vials. To monitor accuracy, USGS reference rock powders (geostandards) AGV-2 and BHVO-1 with known Fe isotope compositions (Craddock and Dauphas, 2011) were processed and analyzed alongside the samples. Samples were digested in the Teflon vials using concentrated mixtures of acid on hot plates: i) 1.5 mL of 2:1 HF-HNO3 for 5 h at 100 °C; (ii) 1.25 mL of 3:1 HCl-HNO3 (aqua regia) overnight at 140 °C; (iii) 1.5 mL of 2:1 HCl-HNO3 overnight at 140 °C; (iv) 1 mL HCl at 180 °C for 48 h. Each digestion step was followed by thorough drying with open vials at 120–130 °C. The final dried samples were then dissolved in 0.5 mL of 6 M HCl for Fe separation via column anion-exchange chromatography.

Bio-Rad Poly-prep columns were filled with  ${\sim}1$  mL of BioRad AG1-X8 200-400 resin conditioned by following to the procedure outlined by Dauphas et al. (2004). The samples were then loaded into the columns where the matrix and interfering elements were eluted by passing 9 mL of 6 M HCl. The concentrated Fe in the columns was recovered in Teflon beakers with 8 mL of 0.4 M HCl. This process was repeated after sample evaporation and dissolution in 0.5 mL of 6 M HCl. The eluted solutions were then evaporated and refluxed overnight in concentrated HNO3 at 140 °C. Samples were evaporated again to a small drop (<25  $\mu$ L) and finally dissolved at 130 °C in 5 mL of 0.3 M HNO3 for isotopic analyses.

Fe isotope ratio measurements were performed on a Thermo Scientific NeptunePlus Multi-Collector Inductively-Coupled-Plasma Mass-Spectrometer (MC-ICP-MS). High-resolution mode was used to resolve mass interferences between Fe and argides. A standard Ni sampler and Ni H-type skimmer cones were used along with a static cup configuration that enabled simultaneous measurement of masses 53–60. This mass range included all four Fe isotopes, as well as  $^{53}\mathrm{Cr},\,^{55}\mathrm{Mn},\,^{59}\mathrm{Co},\,$  and  $^{60}\mathrm{Ni}.$  Interferences caused by  $^{54}\mathrm{Cr}$  on  $^{54}\mathrm{Fe}$  and  $^{58}\mathrm{Ni}$  on  $^{58}\mathrm{Fe}$  were corrected by measuring  $^{53}\mathrm{Cr}$  and  $^{60}\mathrm{Ni}$  isotopes. Sufficient separation of Fe

from matrix elements during column chemistry was validated by monitoring  $^{55}$ Mn and  $^{59}$ Co, and Mn/Fe and Co/Fe ratios were always below  $3 \times 10^{-6}$  and  $7 \times 10^{-7}$ , respectively. Each Faraday cup was assigned  $10^{11}$   $\Omega$  feedback resistors, with the exception of the  $^{60}$ Ni (H4-F) cup, which utilized a  $10^{12}$   $\Omega$  resistor to improve Ni isobaric interference corrections. Amplifier gain calibration was performed at least weekly.

Samples and standard solutions were introduced into the mass spectrometer as an aerosol at a nominal flow rate of 50  $\mu L/\text{min}$  using a PFA nebulizer coupled with a glass spray chamber. The solutions were diluted to 5  $\mu g/g$  in 0.3 M HNO3, which resulted in beam intensities of 20–25 V on  $^{56}\text{Fe}$ : a sensitivity of 4–5 V/ppm of Fe. To monitor system memory effects of the sample introduction system and establish baselines, on-peak-zeros (OPZ) were acquired before all unknown and standard solution measurements. These measurements involved a 90 s sample uptake and 40 s on-peak acquisition, using a clean acid solution from the same batch used to dilute the samples. The typical background intensity recorded was  $\sim\!10^{-5}\,\text{V}$  on  $^{56}\text{Fe}$ .

Isotopic fractionation due to instrumental shift was corrected by standard bracketing, using the IRMM-524a metallic iron standard as reference material. The standard solution was diluted in the same batch of acid as the unknown samples and geostandards at a concentration of 5  $\,\mu g/g$  concentration ( $\pm 5$ %). Sample measurement procedure consisted of a 90 s sample uptake, followed by 50 cycles of data acquisition, each with an integration time of 4.192 s, which yields 210 s of continuous onpeak measurement. After each measurement, the inlet system was rinsed for 120 s using 3 vol% HNO3. Along with the unknown samples, one of the two geostandards was measured within each analysis session.

Each reported sample composition is the arithmetic mean of n replicates measured during the same analysis session (typically between 5 and 9). The analytical uncertainties reported here are 95 % confidence intervals calculated as  $2 \times \sigma_{std}/\sqrt{n}$ , where  $\sigma_{std}$  is the standard deviation of repeat measurements of the IRMM-524a standard bracketed by itself during the session (Dauphas et al., 2009). This approach provides an accurate estimate of variability across the entire analysis session. However, for reference, we also calculated uncertainties as two times the standard error (SE), where SE is calculated as  $\sigma_{sample}/\sqrt{n}$ . These estimates were lower or similar to the uncertainties estimated using the bracketing standard, indicating consistent measurements during individual sample analyses.

All the collected iron isotope data were expressed relative to IRMM-524a in delta notation in terms of  $\delta^{56}\text{Fe}$  and  $\delta^{57}\text{Fe}$ . We measured the iron isotope composition of IRMM-524a using the well-characterized IRMM-014 reference material as the bracketing standard (Taylor et al., 1992). The average  $\delta^{56}\text{Fe}$  and  $\delta^{57}\text{Fe}$  obtained were  $+0.005\pm0.018$ %% and  $-0.003\pm0.026$ %, respectively (n=59), confirming that IRMM-524a is isotopically identical to IRMM-014 within analytical uncertainty (Craddock and Dauphas, 2011). We subsequently discuss our results using only  $\delta^{56}\text{Fe}$ , since all data are mass-dependent (i.e.,  $\delta^{57}\text{Fe}=1.5~\text{x}$   $\delta^{56}\text{Fe}$ ; Supplementary Fig. S1).

# 4.4. Phase equilibrium modeling

Phase equilibrium modeling was used to estimate mineral and melt proportions and compositions during partial melting. The calculations were performed using the software Theriak-Domino at fixed pressures of 0.3 and 0.4 GPa and a temperature range of 600–1000 °C. We used the compositional system MnO-Na<sub>2</sub>O-K<sub>2</sub>O-CaO-FeO-MgO-Al<sub>2</sub>O<sub>3</sub>-SiO<sub>2</sub>-H<sub>2</sub>O-TiO<sub>2</sub>-O<sub>2</sub> (MnNKCFMASHTO), which is appropriate for partial melting of metasedimentary rocks (White et al., 2014b). The thermodynamic dataset we selected includes the internally consistent database of Holland and Powell (2011) and activity-composition (*a-x*) relations appropriate for typical stable phases during anatexis of metapelites: biotite (Bt), garnet (Grt), cordierite (Crd), orthopyroxene (Opx), chlorite (Chl), and staurolite (St) (White et al., 2014b), silicate melt (Melt) and white mica (Ms) (White et al., 2014a), ilmenite-hematite (Ilm-Hem)

(White et al., 2000), spinel-magnetite (Spl-Mag) (White et al., 2002), plagioclase (Pl) and K-feldspar (Kfs) (Holland and Powell, 2003), and epidote (Ep) (Holland and Powell, 2011). Pure phases include quartz (Qtz), rutile (Rt), titanite (Ttn), sillimanite (Sil), andalusite (And), kyanite (Ky), and hydrous fluid ( $\rm H_2O$ ). The mineral abbreviations herein are from (Warr, 2021).

We focused on partial melting occurring at minimally saturated water conditions (~0.5 mol% H<sub>2</sub>O at the solidus), which avoids unconstrained overestimation of the melt fraction with fluid-present melting. However, phase equilibrium calculations were also conducted under water-undersaturated and water-excess conditions for reference. We performed calculations with oxygen fugacity buffered at FMQ+2, FMQ, and FMQ-2, where FMQ corresponds to the favalite-magnetitequartz buffer. Because the a-x model for silicate melt has no ferric iron component, we independently estimated the  $\mathrm{Fe}^{3+}/\Sigma\mathrm{Fe}$  proportion of the calculated melt phase using the algorithm from Kress and Carmichael (1991). We note that different models have been proposed for the estimation of  $Fe^{3+}/\Sigma Fe$  ratios in silicate melts based on their composition (e.g., Kress and Carmichael, 1991; Borisov et al., 2015; O'Neill et al., 2018), but none of these have been calibrated for felsic systems. We preferred the Kress and Carmichael (1991) parametrization as, unlike the other models, all the required chemical components are included in the melt a-x relationships from White et al. (2014a).

# 4.5. Isotopic fractionation during partial melting

Quantitative estimates of isotopic fractionation due to partial melting were calculated using phase equilibrium modeling. For each Febearing phase predicted to be in equilibrium at a given temperature, a force constant [F] was assigned a constant value or calculated using a composition-dependent expression compiled from the literature (see Table 1). Since no force constants have been measured for cordierite, we assumed the same value as that of biotite without ferric iron since both are aluminosilicates with mostly  $\mathrm{Fe^{2+}}$  ( $\mathrm{Fe^{3+}}/\mathrm{\Sigma Fe} < 0.1$ ) accommodated in octahedral sites in reduced granites and (meta-)sedimentary rocks (Guidotti and Dyar, 1991; Khomenko et al., 2001; Bucholz et al., 2018).

A bulk value of [F] for the residue was calculated as the weighted average of all solid phases, using the formula  $\sum_{i=1}^{n} F_i \times p_i$ , where  $F_i$  and  $p_i$  are the force constant and molar proportion of phase i, respectively, and n is the number of iron-bearing phases in the system at a given temperature. For solid solutions phases whose force constant is defined for one of the endmembers, their molar proportion was adjusted to the content of that endmember in the phase. For instance, if biotite and garnet are present at 70 mol% and 30 mol%, respectively, with 60 %

**Table 1** Force constants for Fe-carrying phases.

Phase	Force constant (N/m)	Method	Reference	
Silicate melt	$\left[199 + \frac{41}{1 + e^{34 - SiO_2}}\right] \times $	NRIXS	(Dauphas et al., 2014)	
	$\left(1 - \frac{Fe^{3+}}{\Sigma Fe}\right) + 351  imes \left(\frac{Fe^{3+}}{\Sigma Fe}\right)$			
Biotite (Annite)	$188 + 59.4  imes \left(rac{Fe^{3+}}{\Sigma Fe} ight)$	NRIXS	(Nie et al., 2021)	
Garnet (Almandine)	110	NRIXS	(Nie et al., 2021)	
Cordierite	188	-	Same as biotite with no Fe <sup>3+</sup> / $\Sigma$ Fe*	
Ilmenite	$133  imes \left(1 - rac{Fe^{3+}}{\Sigma Fe} ight) + 244  imes \ \left(rac{Fe^{3+}}{\Sigma Fe} ight)$	NRIXS	(Nie et al., 2021)	
Spinel	$\left(\frac{\Sigma Fe}{Fe}\right)$ $196 + 104 \times \left(\frac{Fe^{3+}}{\Sigma Fe}\right)$	NRIXS	(Roskosz et al., 2015)	
Orthopyroxene	177	NRIXS	(Dauphas et al., 2012)	

annite in biotite and 80 % almandine in garnet, the recalculated  $p_{biotite}$  and  $p_{garnet}$  would be 64 % and 36 %, respectively. From  $[F]_{melt}$  and  $[F]_{residue}$ , the fractionation factor between coexisting melt and solid residue ( $\Delta^{56}Fe_{melt-residue}$ ) was then obtained over the temperature interval of interest in terms of delta notation using the expression from Dauphas et al. (2014):

$$\Delta^{56} F e_{melt-residue} = \delta^{56} F e_{melt} - \delta^{56} F e_{residue} = 2853 \times \frac{[F]_{melt} - [F]_{residue}}{T^2}$$
 (1)

The values for  $\delta^{56} Fe_{melt}$  and  $\delta^{56} Fe_{residue}$  were then calculated assuming mass balance in a closed system.

# 5. Results

# 5.1. Petrography and geochemistry

#### 5.1.1. Granites

Bulk-rock major and trace elements and petrographic descriptions for granitic samples are given in Tables S1 and S2, respectively. The location from which these samples were collected is shown in Fig. 2b. The granite samples vary between medium- to coarse-grained granites (sensu stricto) and pegmatitic granites with variable proportions of Kfeldspar, quartz, and plagioclase and other Al-bearing phases such as garnet, tourmaline, sillimanite, cordierite, biotite, or muscovite. The granite samples from the GLB are strongly peraluminous, with all samples displaying ASI values higher than  $\sim$ 1.1. On an anhydrous basis, the silica contents and total alkalis (Na<sub>2</sub>O +  $K_2$ O) range  $\sim$ 72–76 wt% and ~6-10 wt%, respectively. Also, samples are alkali-calcic to alkalic with the modified alkali-lime index (MALI; Na<sub>2</sub>O + K<sub>2</sub>O - CaO; Frost et al., 2001) varying between  $\sim$ 4–9 wt% and K<sub>2</sub>O/Na<sub>2</sub>O ratios  $\sim$ 0.5–2.5. FeO<sub>T</sub> + MgO + TiO<sub>2</sub> values for most granite samples vary between 0.7-1.8 wt% (FeOt = FeO +  $0.9 \cdot \text{Fe}_2\text{O}_3$ ), however the cordierite-bearing sample SP-16-19 has 4.2 wt%. This sample also has higher ASI and lower MALI values than other samples (1.47 and 3.80, respectively) and higher Na<sub>2</sub>O/K<sub>2</sub>O (2.4 compared to <1.5 in other samples). In general, the granite samples from the GLB show medium to low CaO/Na2O and intermediate to high Al<sub>2</sub>O<sub>3</sub>/TiO<sub>2</sub> compared to other peraluminous granites (Fig. 3a). The Al<sub>2</sub>O<sub>3</sub>/TiO<sub>2</sub> and CaO/Na<sub>2</sub>O ratios are inversely correlated, and the selected samples from the GLB follow a trend similar to that of other Archean and Proterozoic strongly peraluminous granites (Fig. 3a).

# 5.1.2. Metasedimentary rocks

Bulk-rock major and trace elements and petrographic descriptions for metasedimentary samples from the Zealand unit are also summarized in Tables S1 and S2. These rocks include micaceous phyllites from the biotite-chlorite zone, quartz-feldspathic schists with biotite  $\pm$  garnet from the andalusite and garnet zones, quartz-feldspathic gneisses with biotite, muscovite, sillimanite  $\pm$  andalusite from the sillimanite and sillimanite-K-feldspar zones, the latter of which shows evidence of incipient partial melting. The SiO2 and Al2O3 of the analyzed metasedimentary rocks range ~54-64 wt% and ~16-22 wt%, respectively, with more pelitic samples having lower SiO<sub>2</sub> and higher Al<sub>2</sub>O<sub>3</sub> (Fig. 4). However, the metasedimentary rocks broadly contain intermediate molar Al<sub>2</sub>O<sub>3</sub> compared to a global compilation of pelitic rocks (Forshaw and Pattison, 2022; Fig. 4a-b). For most samples, FeO<sub>T</sub> and MgO contents are positively correlated and vary between ~5–9 wt% and ~2.5–4 wt%, respectively, following the trend defined by the global compilation of metapelites. The two exceptions are samples SP-16-11 and SP-18-27, with high FeO contents (10.9-12.3 wt%), reflecting the presence of abundant sulfide grains in the former and ilmenite in the latter.

# 5.2. Iron isotopes

Fig. 5 and Table 2 summarize the iron isotope measurements for the

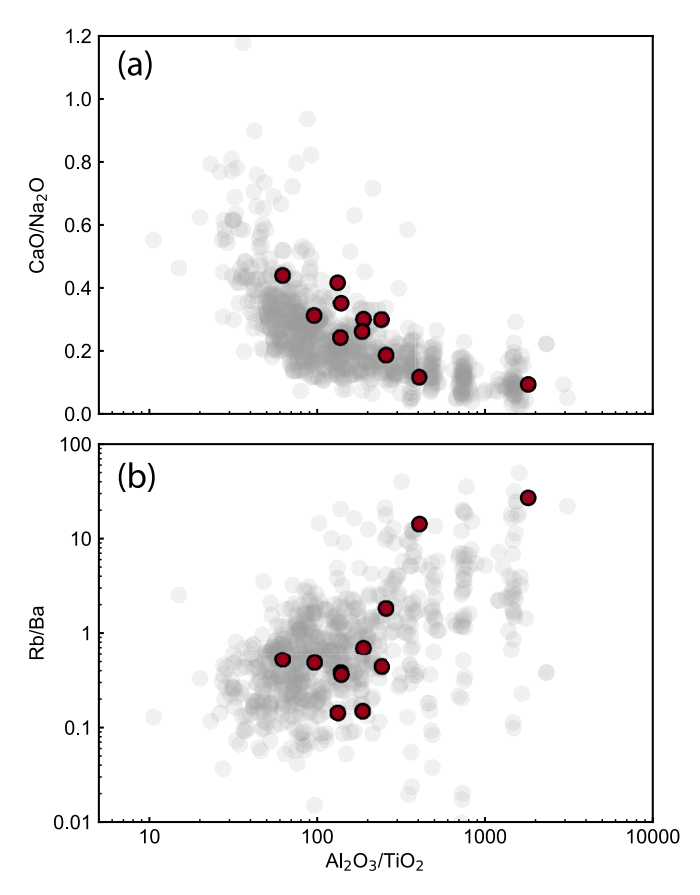


**Fig. 3.** Major and trace element ratios for samples from the GLB. Filled red circles are individual granite samples. The light gray circles correspond to compositions from a global compilation of Archean and Proterozoic SPGs by Bucholz and Spencer (2019). a) CaO/Na $_2$ O versus Al $_2$ O $_3$ /TiO $_2$  and b) Rb/Ba versus Al $_2$ O $_3$ /TiO $_2$ .

granite, metapelite, restite, sulfide, and geostandard samples. The measured  $\delta^{56} \text{Fe}$  values for geostandard samples are identical, within uncertainty, to the reference values recommended by Craddock and Dauphas (2011). Granite samples have  $\delta^{56} \text{Fe}$  values spanning  $+0.111 \pm 0.018$ % and  $+0.315 \pm 0.038$ %, averaging +0.192%. Overall, granites are isotopically heavier than the average of the metapelites, although there is some overlap in the lower end of the granite  $\delta^{56} \text{Fe}$  values (Fig. 5). Notably, the granite samples from the inclusion-rich zone in GLB-1 tend to be isotopically heavier with  $\delta^{56} \text{Fe}$  ranging from +0.194 to +0.315%. No apparent correlation exists between granite units and measured  $\delta^{56} \text{Fe}$  values (Fig. 5).

The  $\delta^{56}$ Fe of the metasedimentary samples ranges from  $-0.188 \pm$ 0.023 % to +0.191  $\pm$  0.035 %, averaging +0.101 % (or +0.130 % when excluding SP-16-11). Although there is no correlation between measured  $\delta^{56}$ Fe compositions and increasing metamorphic grade (Fig. 5), it is noteworthy that the two samples from the sillimanite zone have the heaviest isotopic composition. In contrast, samples from the garnet zone display the lowest  $\delta^{56}$ Fe values. SP-16-43 and SP-16-44 represent an andalusite-bearing interbedded metapelite and metawacke, respectively, with incipient replacement of andalusite by sillimanite. The two samples were sampled within a meter of each other and have, within error, the same isotopic composition:  $\delta^{56}$ Fe +0.191  $\pm$ 0.035 % and  $+0.189 \pm 0.037$  %, respectively. The samples from the garnet zone were interbedded with banded iron formations in the Zealand unit. These samples show  $\delta^{56}$ Fe ranging from -0.188 to +0.114 ‰, where sample SP-16-11 has the lightest isotopic composition,  $\delta^{56}$ Fe =  $-0.188 \pm 0.023$  %, consistent with the presence of abundant isotopically light sulfides (see sulfide results below), while the other two samples, SP-18-26 and SP-18-27, have  $\delta^{56} Fe$  of  $+0.004 \pm 0.043$  % and

 $+0.114\pm0.035$  %, respectively. Samples SP-18-5, SP-18-6, and SP-18-8, from the biotite–chlorite zone, show a 0.08 % range in  $\delta^{56} Fe$  with values of  $+0.166\pm0.044$  %,  $+0.086\pm0.044$  %, and  $+0.134\pm0.038$  %, respectively. By contrast, SP-16-16 and SP-18-34, from the sillimanite–K-feldspar zone, and SP-16-37, from the andalusite zone, display isotopic compositions intermediate to the range observed in the biotite-chlorite zone with  $\delta^{56} Fe+0.119\pm0.037$  %,  $+0.144\pm0.017$  %, and  $+0.147\pm0.018$  %, respectively. Finally, the restitic sample SP-16-30 has  $\delta^{56} Fe=0.000\pm0.043$  %.

Sulfide grains display significant isotopic variability among samples. The lightest composition corresponds to pyrrhotite in sample SP-16-11 with  $\delta^{56}\text{Fe}$  of  $-0.337\pm0.025$  ‰. By contrast, pyrrhotite in metapelite samples SP-16-16, SP-18-26, and SP-18-27 have  $\delta^{56}\text{Fe}$  of  $+0.198\pm0.044$  ‰,  $+0.364\pm0.044$  ‰, and  $+0.337\pm0.044$  ‰, respectively. Finally, granite sample SP-16-20a has pyrrhotite with a  $\delta^{56}\text{Fe}$  of  $+0.109\pm0.025$  ‰.

# 5.3. Phase equilibrium modeling

Fig. 6 shows the results of phase equilibrium calculations for sample SP-16-16 within a temperature range of  $600-1000\,^{\circ}\mathrm{C}$  and constant pressure of 0.4 GPa, interpreted to be the approximate peak pressure of metamorphism for the metasedimentary rocks that comprise the Zealand unit. Sample SP-16-16 was selected for modeling as it is a representative composition of the metasedimentary rocks of the Zealand Unit (Fig. 4). The modeling results described here are relevant for closed system conditions (batch melting), where all the stable phases are in equilibrium with each other at any given temperature. Modeling results at different conditions of the system are presented and discussed in the Supplementary Material. This includes results at 0.3 GPa (Fig. S2) and initial  $\mathrm{H_{2}O}$  contents corresponding to water-undersaturated and water-excess conditions at the solidus (Fig. S3). We also include results for partial melting considering melt extraction each time the system reached a critical melt fraction of 7 vol% (Fig. S4).

Phase stability is similar between the FMQ-2 and FMQ model runs, with only minor variations in stability fields and higher Fe $^{3+}/\Sigma Fe$  for phases incorporating ferric iron in the FMQ model (Fig. 6a–f). For simplicity in the discussion, we consider the model results run at FMQ-2 and FMQ first and discuss the results of the model run at FMQ+2 later. Under these lower oxygen fugacity conditions, partial melting starts with  $\rm H_2O$  release from biotite dehydration at  $\sim\!670$  °C, which reacts with quartz and plagioclase to produce melt (Spear, 1993). Production of melt via this reaction is minimal, and iron concentrations in the produced granitic melt are low ( $<\!\sim\!0.25$  wt% on an anhydrous basis). At  $\sim\!700$  °C, melting continues via the reaction:

$$Bt + Sil + Qtz = Melt + Crd + Kfs \pm Ilm$$
 (2)

which takes place until sillimanite is exhausted at  $\sim\!725\,^{\circ}\text{C}.$  During this melting interval, most of the iron is accommodated in cordierite, ilmenite, and biotite, and only a negligible amount is transferred to the melt. From  $\sim\!725\text{--}750\,^{\circ}\text{C}$ , a small quantity of melt is produced due to plagioclase reaction with quartz. Then, at  $\sim\!750\,^{\circ}\text{C}$ , garnet is introduced to the mineral assemblage via the reaction:

$$Bt + Qtz + Pl = Melt + Grt + Crd + Ilm$$
(3)

Reaction (3) proceeds until  $\sim$ 810 °C, increasing the amount of melt to  $\sim$ 30 mol% and transferring  $\sim$ 5 % of the bulk Fe in the system to the melt. Finally, orthopyroxene becomes stable in the residual assemblage at 815 °C, and the melt fraction increases to  $\sim$ 36 mol% when biotite is quickly consumed through reaction (4):

$$Bt + Qtz + Grt = Melt + Opx + Crd + Ilm$$
 (4)

For temperatures above 815 °C, melt and orthopyroxene are steadily produced by feldspar reaction with quartz and garnet. Then, at  $\sim$ 930 °C, spinel becomes stable, and the melt-producing reaction rapidly

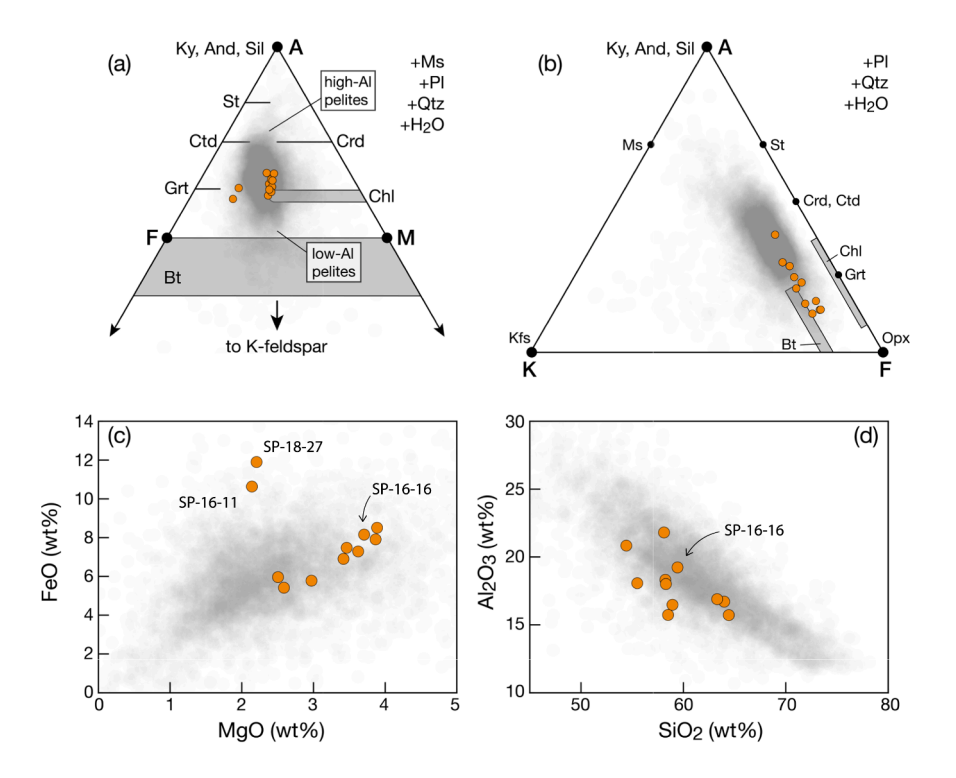


Fig. 4. Compositional features of metasedimentary rocks from the Zealand unit. Filled orange circles are individual samples. The shaded regions are data points from a global compilation of metapelites from Forshaw and Pattison (2022). (a) AFM ternary diagram —  $A = \text{molar Al}_2O_3 - 3*K_2O$ ;  $F = \text{molar FeO}_t$ ; M = molar MgO. (b) AKF ternary diagram —  $A = \text{molar Al}_2O_3 - (\text{Na}_2O + K_2O + \text{CaO})$ ;  $K = \text{molar K}_2O$ ;  $F = \text{molar FeO}_t + \text{MgO}_t + \text{M$ 

consumes quartz and garnet until garnet runs out at  $\sim$ 950 °C. Melt and spinel then continue to be produced through the reaction of orthopyroxene with plagioclase, reaching a total melt fraction of  $\sim$ 80 mol% with  $\sim$ 55 % of Fe in the bulk system residing in the melt at 1000 °C (Fig. 6a–f).

The subsolidus mineral assemblage and initial melting reaction for the most oxidized model (i.e., FMQ+2) are the same as for lower oxygen fugacity calculations. At  $\sim\!720\,^{\circ}\text{C}$ , melt is produced through reaction (1) until sillimanite is entirely consumed at  $\sim\!730\,^{\circ}\text{C}$ . The formation of spinel (magnetite) and ilmenite at  $\sim\!725\,^{\circ}\text{C}$  quickly consumes biotite and increases the rate of melt production. Biotite readily disappears at  $\sim\!825\,^{\circ}\text{C}$  when orthopyroxene joins the mineral assemblage via reaction (4), with the proportion of melt increasing to  $\sim\!30$  mol%. Orthopyroxene and melt are then produced by the reaction of feldspar with quartz, magnetite, and cordierite, which eventually consumes all the available quartz and K-feldspar. Melt generation continues at the expense of plagioclase and orthopyroxene, reaching  $\sim\!80$  mol% melt at 1000 °C (Fig. 6g–i).

The subsolidus equilibria and partial melting products at a constant pressure of 0.3 GPa closely resemble those predicted at 0.4 GPa, with the most notable differences related to cordierite and garnet stability. At 0.3 GPa, the stability field of cordierite extends to temperatures below the solidus, replacing sillimanite and increasing its modal proportion relative to other iron-bearing phases. The main partial melting reaction can be written as follows:

$$Bt + Crd + Qtz \pm Pl = Melt + Kfs \pm Grt \pm Ilm$$
 (5)

which proceeds until biotite is exhausted at  $\sim$ 790 °C. Notably, reaction (5) produces only a small amount of garnet, which is quickly consumed by reaction (4) before biotite depletion. While reactions (4) and (5) increase the melt fraction from  $\sim$ 10 mol% to  $\sim$ 30 mol% between  $\sim$ 780–790 °C, less than  $\sim$ 5% of the bulk Fe in the system is in the melt. Melt production then continues via the reaction of feldspar with quartz,

where orthopyroxene and cordierite are the peritectic phases. When quartz is used up at ~835 °C, melt is produced by reaction between feldspar and orthopyroxene, with cordierite remaining relatively stable.

#### 5.4. Equilibrium fractionation of iron isotopes

Since the phase relationships for a system with oxygen fugacity conditions varying from FMQ-2 to FMQ are nearly identical, the lines defined by the resulting fractionation factors between the melt phase and complementary residual solid vs temperature trajectories are almost parallel across the whole temperature range considered (Fig. 7). The model run at FMQ is offset  $\sim$ 0.04 % towards higher  $\Delta^{56}$ Fe<sub>melt-residue</sub> relative to FMQ-2 due to the greater proportion of Fe<sup>3+</sup> in the melt. By contrast, the fractionation factors vs temperature trajectories for melts produced at the FMQ+2 buffer only parallels the more reduced models at the onset of partial melting (Fig. 7). At the solidus, the estimated  $\Delta^{56}$ Fe<sub>melt-residue</sub> values are ~+0.225, ~+0.290, and ~+0.450 % for the FMQ-2, FMQ, and FMQ+2 models, respectively. These values then decrease nearly monotonically until garnet enters the mineral assemblage at  $\sim$ 750 °C (Fig. 7). From this temperature, the increase in  $\Delta^{56}$ Fe<sub>melt-residue</sub> reflects the continued loss of biotite from the solid assemblage and the increasing modal proportion of garnet ([F] =  $110 \, \text{N}/$ m) relative to biotite ([F] > 188 N/m). With biotite exhausted, the modeled  $\Delta^{56} Fe_{melt\text{-residue}}$  drops by  ${\sim}0.03$  ‰ and then decreases at a constant rate from  $\sim\!815\,^{\circ}\text{C}$  to  $\sim\!930\,^{\circ}\text{C}$ . Garnet is consumed when spinel joins the mineral assemblage, and cordierite and orthopyroxene decrease their proportions, further decreasing melt-residue fractionation (Fig. 7).

In contrast, for the model run at FMQ+2, sillimanite replacement by cordierite coincides with ilmenite and spinel joining the mineral assemblage, while biotite is rapidly consumed (Fig. 7). This results in an abrupt transition to lower  $\Delta^{56} Fe_{melt\text{-residue}}$  values, which decrease at a relatively constant rate due to the replacement of biotite by orthopyroxene at  $\sim\!825~^\circ\text{C}$  and a decrease in the modal abundance of magnetite

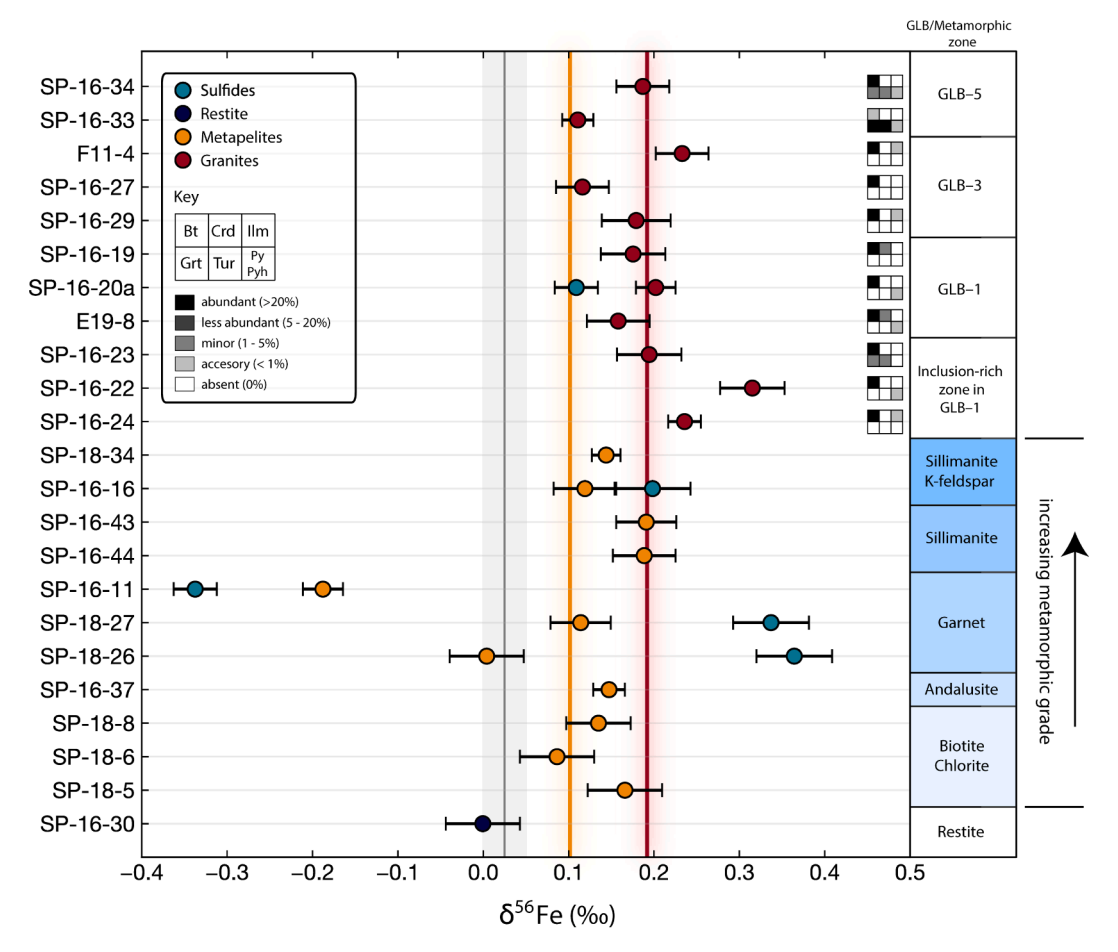


Fig. 5.  $\delta^{56}$ Fe of rocks from the GLB and the Zealand unit. Bulk-rock analyses of granite samples are shown in red, metapelites in orange, and the restite in dark blue; sulfides from four metapelites and a granite sample are shown in green. Colored vertical lines are averages for granites (red) and metapelites (orange). The grey vertical region is the average mantle composition ( $+0.025 \pm 0.025$  %; Craddock et al., 2013). The presence and abundance of iron-bearing minerals for granite samples are shown qualitatively in the square grid diagrams. Mineral abundance was visually estimated from thin sections using a reference chart for modal proportions (Terry and Chilingar, 1955). The GLB zones for granite samples and metamorphic zones for metapelites are shown in the columns to the right.

(modeled as an endmember of the spinel solid-solution). Finally, the  $\Delta^{56} Fe_{melt\text{-residue}}$  gradually decreases for temperatures above  ${\sim}825~^{\circ}\text{C}$  since the distribution of solid Fe-bearing phases remains relatively constant at these temperatures.

# 6. Discussion

#### 6.1. Iron isotopes in the metasedimentary source rock

Mineral heterogeneity in the sedimentary protolith (e.g., relative abundance of clay versus feldspars) of the Zealand unit metasedimentary rocks can be translated into variable isotopic compositions upon metamorphism, which in turn can be transferred to the melt during anatexis. Indeed, the Zealand unit metasedimentary rocks display a range of isotopic compositions consistent with the variability in the GLB samples. However, the relationship between the mineralogy and isotopic composition of the Zealand unit samples is complex and particular to each sample. For instance, sample SP-16-11 has the lowest  $\delta^{56}$ Fe, resulting from its high modal proportion ( $\sim$ 10–15 %) of pyrrhotite with  $\delta^{56}$ Fe<sub>po</sub> =  $-0.337 \pm 0.025$  %, which is also reflected in a high FeO/MgO compared to other metapelites (Fig. 4c). Sample SP-18-27 also has elevated FeO/MgO, consistent with abundant ilmenite observed in that sample; however, ilmenite drives this sample towards a positive bulk  $\delta^{56}$ Fe value (+0.114  $\pm$  0.035 %). Sample SP-18-26, collected from the same location as SP-18-27, in contrast, contains garnet and biotite as main iron carriers, and its isotopic composition is thus lighter ( $\delta^{56}$ Fe =

 $+0.004\pm0.043$  %). Both SP-18-27 and SP-18-26 contain similar proportions of biotite and garnet and only minor pyrrhotite, which, while having elevated  $\delta^{56}$ Fe ( $+0.364\pm0.044$  % and  $+0.337\pm0.044$  %; Fig. 5; Table 2), exerts little control on the bulk-rock  $\delta^{56}$ Fe. Therefore, the large isotopic difference between these two samples is attributed to the significant presence of ilmenite in SP-18-27. It is also worth noting that garnet plays an essential role in the isotopic composition of samples from the Zealand unit. Since most iron in garnet is located in a cubic site, with high coordination number, garnet preferentially partitions light iron isotope species. Thus, samples in which garnet is lacking (or occurs in relatively low amounts) tend to show heavier isotopic compositions (>+0.119 %).

Isotopic heterogeneities in the metasedimentary source of the GLB can result from metamorphism starting at low grade and culminating in partial melting. During prograde metamorphism, iron is generally mobilized between different phases through metamorphic reactions from lower-greenschist to granulite facies (Slotznick et al., 2018). Fractionation of iron isotopes is, therefore, a natural outcome of the metamorphic process. However, the magnitude and direction of the isotopic fractionation will depend on the  $P\!-\!T$  conditions, the stable mineral assemblages, and the extent of fluid exchange within and out of the system (Valley, 1986). For rocks from the Zealand unit, there is no apparent correlation between metamorphic grade and  $\delta^{56}$ Fe values (Fig. 5), suggesting that increasing  $P\!-\!T$  conditions during prograde metamorphism have a negligible or non-systematic effect on the iron isotope composition of the metasediments.

**Table 2**Iron isotope compositions of granites, metapelites, sulfides, and geostandards.

Lithology	Sample	GLB / Metamorphic Zone	n	δ <sup>56</sup> Fe	95 % c.i.	2 SE	$\delta^{57} Fe$	95 % c.i.	2 SE
Granites	SP-16-34	GLB-5	8	0.187	0.031	0.016	0.266	0.044	0.017
	SP-16-33	GLB-5	5	0.111	0.018	0.009	0.183	0.034	0.024
	F11-4	GLB-3	8	0.233	0.031	0.021	0.349	0.044	0.039
	SP-16-27	GLB-3	8	0.116	0.031	0.018	0.182	0.044	0.026
	SP-16-29	GLB-3	7	0.179	0.040	0.019	0.261	0.058	0.023
	SP-16-19	GLB-1	6	0.175	0.038	0.020	0.273	0.066	0.033
	SP-16-20a	GLB-1	5	0.202	0.023	0.019	0.293	0.048	0.035
	E19-8	GLB-1	9	0.158	0.037	0.019	0.244	0.053	0.030
	SP-16-23	Inclusion-rich zone in GLB-1	6	0.194	0.038	0.021	0.295	0.066	0.030
	SP-16-22	Inclusion-rich zone in GLB-1	6	0.315	0.038	0.013	0.476	0.066	0.028
	SP-16-24	Inclusion-rich zone in GLB-1	7	0.236	0.019	0.013	0.349	0.031	0.018
Metasedimentary rocks	SP-18-34	Sillimanite – K-feldspar	6	0.144	0.017	0.012	0.221	0.026	0.028
	SP-16-16	Sillimanite – K-feldspar	9	0.119	0.037	0.019	0.177	0.053	0.032
	SP-16-43	Sillimanite	7	0.191	0.035	0.023	0.285	0.056	0.035
	SP-16-44	Sillimanite	9	0.189	0.037	0.012	0.274	0.053	0.020
	SP-16-11	Garnet	5	-0.188	0.023	0.008	-0.274	0.039	0.012
	SP-18-27	Garnet	7	0.114	0.035	0.011	0.163	0.056	0.013
	SP-18-26	Garnet	6	0.004	0.043	0.016	-0.001	0.062	0.027
	SP-16-37	Andalusite	6	0.147	0.018	0.010	0.216	0.032	0.017
	SP-18-8	Biotite-Chlorite	6	0.135	0.038	0.012	0.208	0.066	0.019
	SP-18-6	Biotite-Chlorite	9	0.086	0.044	0.008	0.132	0.068	0.009
	SP-18-5	Biotite-Chlorite	9	0.166	0.044	0.017	0.231	0.068	0.028
Restite	SP-16-30	Inclusion in GLB-3	6	0.000	0.043	0.016	0.002	0.062	0.039
Sulfides	SP-18-26	Garnet	8	0.364	0.043	0.020	0.559	0.069	0.040
	SP-18-27	Garnet	8	0.337	0.044	0.018	0.495	0.069	0.027
	SP-16-16	Sillimanite – K-feldspar	8	0.198	0.044	0.056	0.306	0.069	0.090
	SP-16-20a	GLB-1	8	0.109	0.025	0.021	0.186	0.041	0.043
	SP-16-11	Garnet	8	-0.337	0.025	0.019	-0.499	0.041	0.040
	01 10 11	Guinet	Ü	0.007	0.020	0.013	0.155	0.0.12	010 10
	Sample			$\delta^{56} Fe$	2 SE	ref.*	$\delta^{57} Fe$	2 SE	ref.*
Geostandards	AGV-2			0.107	0.002	$0.105 \pm 0.011$ ‰	0.151	0.010	$0.146 \pm 0.016$ %
	BHVO-1			0.105	0.004	$0.105\pm0.008~\%$	0.166	0.009	$0.161 \pm 0.012 \ \%$

ref.\* Craddock and Dauphas (2011).

The role of fluid transfer on iron isotope fractionation during metamorphism may be relatively minimal, although it has yet to be studied in detail. In an open system, prograde metamorphism is dominated by mineral dehydration and fluid loss from the system (Guiraud et al., 2001). An overall decrease of light isotopic species is thus expected as ferrous iron tends to be more soluble in aqueous fluids at metamorphic conditions than ferric iron (Azimov and Bushmin, 2007). If external fluids are introduced, by contrast, retrograde metamorphism will produce hydrated phases, and the isotopic composition of the system will move towards the composition of the fluids. However, large fluid-torock ratios would be required to significantly modify the isotopic composition of the host rock, as most metamorphic fluids typically have low iron contents (i.e., «1 wt%; Yardley, 2005, 2013; Hermann et al., 2013; Yardley and Bodnar, 2014). For example, as much fluid as rock mass must be expelled from (or introduced to) the system to change the  $\delta^{56}$ Fe by  $\pm 0.1$  % (i.e., a fluid-to-rock ratio of  $\sim 2:1-3:1$  in volume). This estimate assumes 1 % and 5 % iron contents and initial  $\delta^{56}$ Fe values of -0.5 % and 0.1 % for the fluid and the rock, respectively (Yardley, 2005; Dauphas et al., 2017).

Progressive metamorphism is generally expected to homogenize isotopic variability given sufficient time at elevated temperatures (Frost et al., 2007; Dauphas et al., 2007a, b; Hyslop et al., 2008). However, the development of metamorphic foliation and the growth of porphyroblasts can result in domains (i.e., bands) with contrasting isotopic compositions and large inter-mineral isotopic heterogeneities, as these processes are accompanied by significant mass transfer (Ague, 1991, 2014). Mineral recrystallization is thus expected to result in the redistribution of isotopic species. Heavier iron isotopes will be preferentially incorporated in phases with low coordination, whereas lighter isotopes will

follow phases with iron in high coordination (Bigeleisen and Mayer, 1947; Urey, 1947; Schauble, 2004). For example, the growth of garnet and biotite at the expense of chlorite, muscovite, and quartz (Spear, 1993) should result in significant isotopic fractionation, producing isotopically light garnet and heavier biotite, while the system composition remains approximately constant. This process is important because the garnet contribution to biotite dehydration melting at the solidus is minimal, which means that the effective source isotopic composition of some SPGs may be heavier than the bulk metasedimentary rock. It is worth noting, however, that inter-mineral equilibrium isotopic fractionation does not always seem to be achieved during burial and metamorphism, or at least not for all phases. For example, some pyrite grains in metasedimentary samples, from prehnitepumpellyite to amphibolite facies, show non-equilibrated  $\delta^{56}$ Fe compositions, consistent with previous studies showing that premetamorphic isotopic signatures can survive high grades of metamorphism (Whitehouse and Fedo, 2007; Galić et al., 2017; Marin-Carbonne et al., 2020; Dupeyron et al., 2023).

Besides iron-bearing aluminosilicates, sulfides are a significant iron pool for metasedimentary rocks. Even small abundances of sulfides can significantly influence the bulk-rock isotopic composition as these phases contain a large amount of iron, and their iron isotope composition can be as variable as several per mil in  $\delta^{56} \text{Fe}$  (Rouxel et al., 2005; Dauphas et al., 2017). Sulfides in metasedimentary rocks from the Zealand unit are dominated by pyrrhotite, likely formed from desulfidation of sedimentary pyrite during metamorphism (Ferry, 1981; Craig and Vokes, 1993). The transformation of pyrite to pyrrhotite requires an overall decrease in the Fe/S ratio, which can be accomplished by introducing dissolved iron in free fluids, reaction with iron-bearing

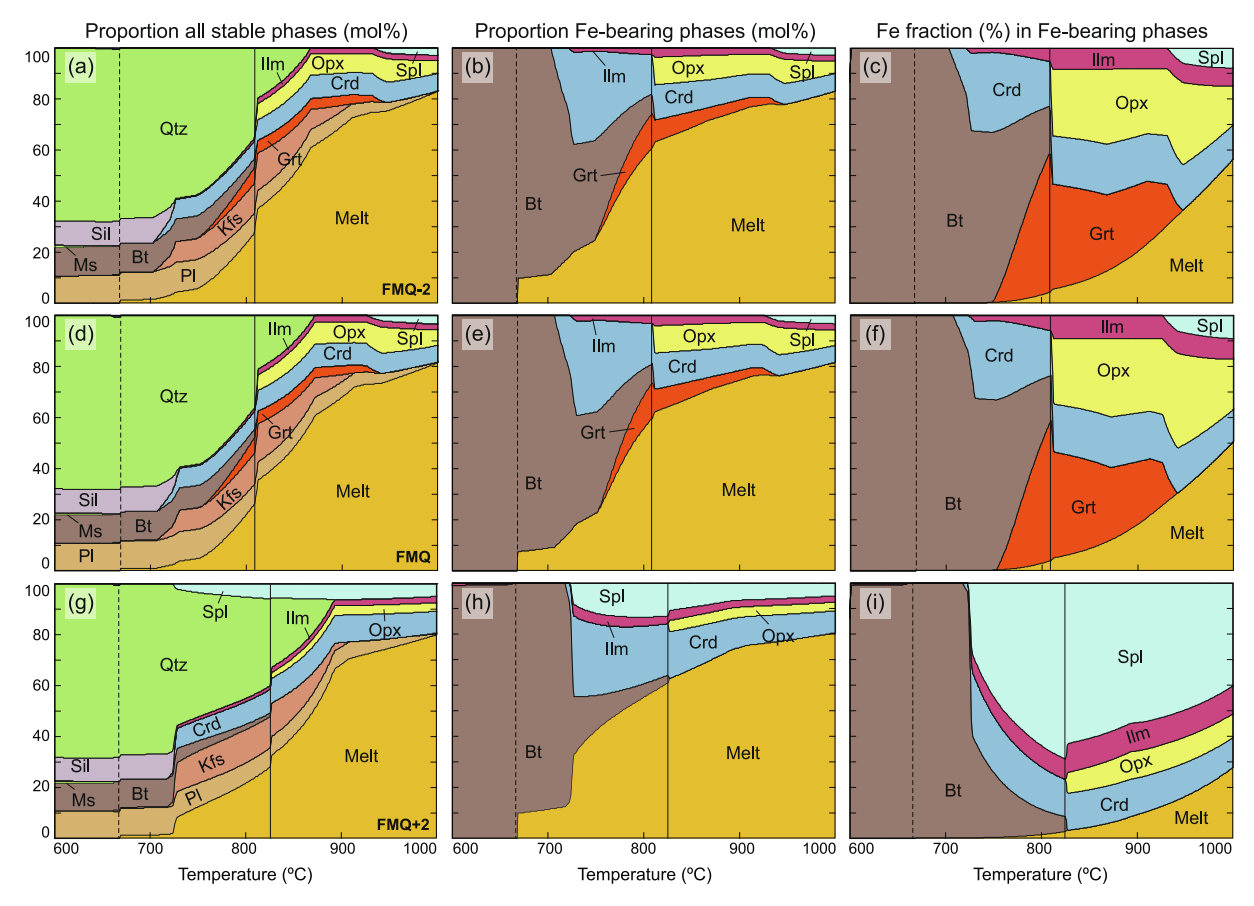


**Fig. 6.** Phase equilibrium modeling results for a metapelite with the composition of sample SP-16-16. The calculations were done at a constant pressure of 0.4 GPa, ranging from 600 °C to 1000 °C under three different oxygen fugacity conditions: FMQ-2 (a–c), FMQ (d–f), and FMQ + 2 (g–i). Panels in the column to the left display the modal proportions in mol% for all the equilibrium phases in the system, the middle column shows the modal proportion in mol% for Fe-bearing phases only, and the column to the right displays the fraction of the total amount of iron in the system that each Fe-bearing phase contains. The vertical dashed line marks the position of the solidus, and the solid line indicates the appearance of orthopyroxene in the mineral assemblage near the end of biotite dehydration melting.

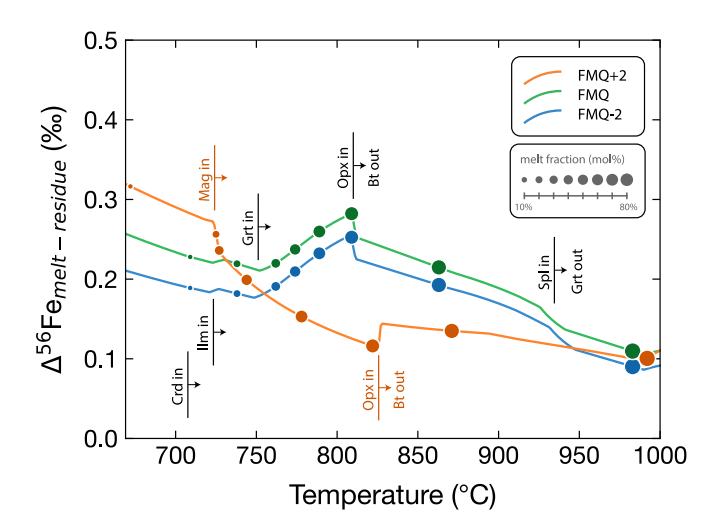


Fig. 7. Predicted iron isotope fractionation between granitic melts and complementary residues produced by partial melting of metapelite SP-16-16 at 0.4 GPa. Oxygen fugacity conditions are FMQ-2 (blue), FMQ (green), and FMQ-2 (orange). Circles with variable sizes represent melt fractions varying from 10 % to 80 %. Vertical lines mark the approximate temperature of orthopyroxene stability and biotite exhaustion.

silicates or oxides, or loss of sulfur to a fluid phase (Ferry, 1981; Craig and Vokes, 1993; Bucholz et al., 2020). The latter is likely the dominant mechanism of pyrrhotite formation in pyrite-poor, mica-rich sediments

because dehydration reactions during prograde metamorphism can drive pyrite breakdown, which requires sulfur loss to maintain equilibrium conditions (Tomkins, 2010; Bucholz et al., 2020). If this is the case, the iron isotope composition of pyrrhotite should be similar to that of its pyrite precursor.

In summary, the relative abundance of iron-bearing phases controls the isotopic composition of metapelites from the Zealand unit. Iron transfer during metamorphic reactions can drive isotopic fractionation between phases and distinct chemical domains formed during metamorphism. However, the bulk sediment will likely preserve a composition similar to that of the protolith (Frost et al., 2007; Dauphas et al., 2007a, b: Hyslop et al., 2008; Marin-Carbonne et al., 2020; Dupeyron et al., 2023). Iron mobility during metamorphism can be regarded as a process occurring under near-closed system conditions, where fluid exchange may contribute minimally to the composition of the metasedimentary rocks. Hence, the range of isotopic compositions of the metasedimentary rocks from the Zealand unit likely represents the compositions of the source sediment and its isotopic variability. Specifically, samples dominated by biotite as the primary iron host, including the restitic sample SP-16-30, are likely close to the effective isotopic composition of the source with  $\delta^{56}$ Fe values between 0 % and 0.191 ‰.

# 6.2. Controls on equilibrium isotope fractionation during anatexis

Before discussing the isotopic composition of granitic rocks from the GLB, it is important to consider the variables that control isotopic fractionation once the system has crossed the solidus. Equilibrium

isotopic fractionation during partial melting can be assessed in terms of variations in force constants, [F], for the melt and its complementary residue. These variations in [F] values reflect changes in the composition of coexisting phases, the mineral assemblage, and oxygen fugacity of the system (Fig. 8a). [F]<sub>melt</sub> decreases with decreasing melt SiO<sub>2</sub> content and  $\mathrm{Fe^{3+}/\Sigma Fe}$ , which occurs as temperature and melt fraction increase. Changes in temperature and melt fraction strongly influence  $\delta^{56}$ Fe<sub>melt</sub>, with maximum fractionation between the melt and the source ranging from  $\sim +0.1$  to +0.3 % (Fig. 8b). Likewise,  $\delta^{56} Fe_{residue}$  only deviates significantly from the source isotopic composition at large melt fractions (Fig. 8b). Mineral  $Fe^{3+}/\Sigma Fe$  ratios and the relative proportion of ironbearing minerals in equilibrium with the melt control the magnitude of [F]<sub>residue</sub>, as this quantity represents a weighted average of the force constants for all the solid phases in the system (Fig. 8c). Thus, isotopic fractionation between the melt and the residue are expected to decrease in a non-monotonic fashion as partial melting progresses (Fig. 8a-b).

#### 6.2.1. Availability of water during melting

The initial water content of the system strongly controls the solidus temperature and the amount and composition of melt produced during partial melting. However, the difference in predicted  $\delta^{56} Fe_{\rm melt}$  values between water-undersaturated and water-saturated models at

equivalent temperatures is relatively small (Supplementary Fig. S5). Additionally, calculated melt compositions under minimally water-saturation conditions at the solidus are consistent with major element and isotopic compositions observed in natural SPGs (see Supplementary Material for discussion). This, along with the observation that fluid-absent reactions dominate the formation of granitic rocks produced by partial melting (Stevens and Clemens, 1993; Clemens et al., 2020), suggests that minimal water-saturation at the solidus is a reasonable assumption for SPG generation. In contrast, while fluid-excess melting may be important for generating leucosomes in some anatectic migmatites, the low pore space in metamorphic rocks restricts the availability of free fluid, thereby limiting the potential for substantial production of granitic rocks through fluid-excess reactions (Stevens and Clemens, 1993).

# 6.2.2. Effects of melt loss

Melt loss events (MLE) in open systems drive changes in the bulk composition of the system during anatexis. Such changes result in different phase compositions and mineral assemblages as compared to batch melting, which translates into distinct isotopic fractionation between the melt and the residue. However, melt extraction during biotite dehydration melting leads to only small differences in  $\Delta^{56} Fe_{melt-residue}$ 

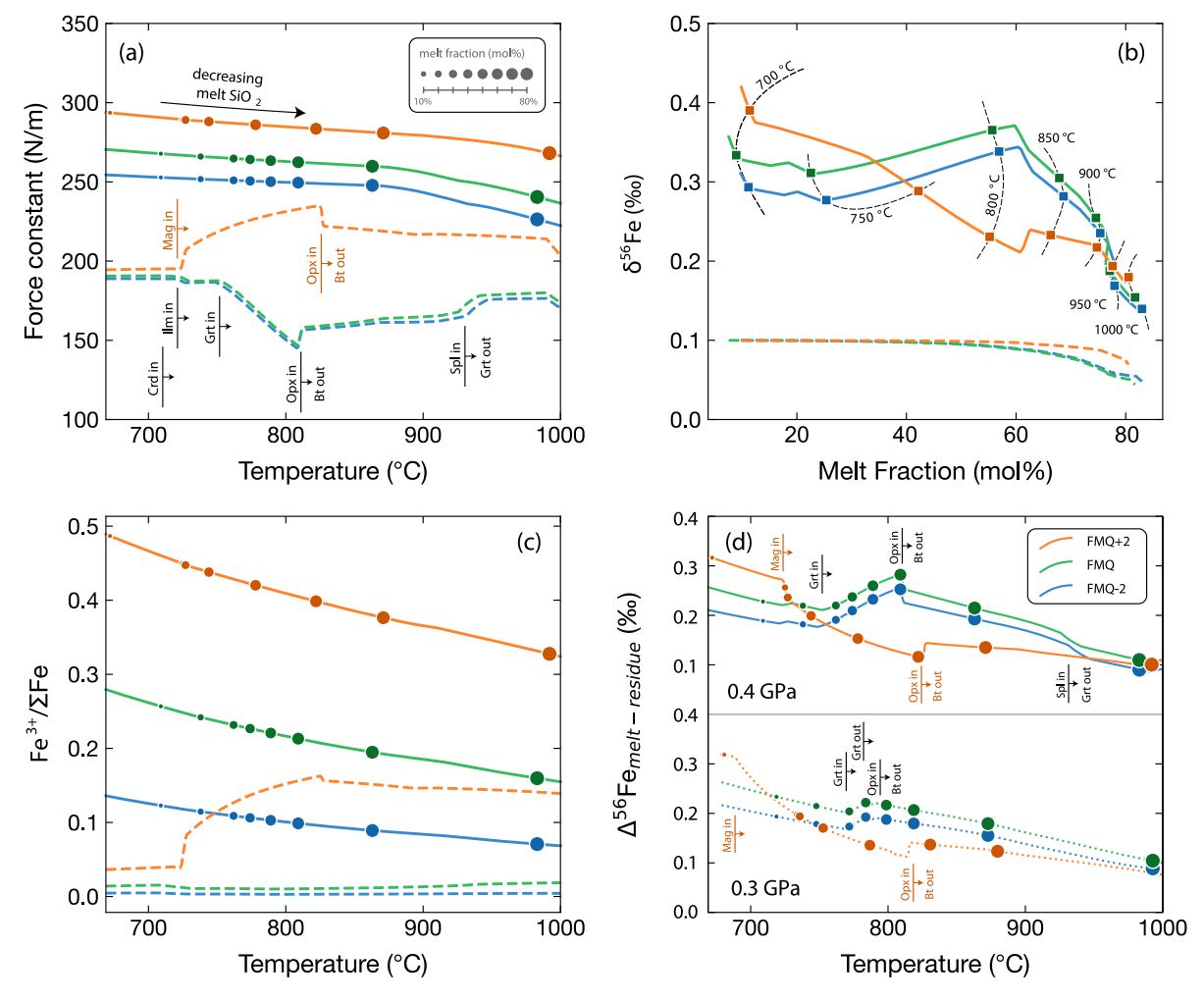


Fig. 8. Variation of parameters relevant to iron isotope fractionation during partial melting of metapelite SP-16-16 at 0.4 GPa. In all panels, continuous lines represent the melt, and dashed lines are the solid residue. The different line colors represent different redox conditions of the system: FMQ-2 (blue), FMQ (green), and FMQ+2 (orange). Circles with variable sizes represent melt fractions varying from 10 % to 80 % in increments of 10 %. (a) Changes in the force constant of the melt phase and the residue as the temperature increases. (b) Relationship between  $\delta^{56}$ Fe, melt fraction, and system temperature. The squares mark the temperature of the system at the corresponding melt fraction. (c) Fe<sup>3+</sup>/ $\Sigma$ Fe for the melt and the solid residue as temperature increases. For the melt, the ferric iron content is estimated using the formulation from Kress and Carmichael (1991), as the thermodynamic model for the melt from White et al. (2014a) do not include Fe<sup>3+</sup>. (d) Difference in  $\Delta^{56}$ Fe<sub>melt-residue</sub> for partial melting at 0.4 GPa (continuous lines) and 0.3 GPa (dotted lines).

values relative to fractionation values predicted for batch melting at equivalent temperatures. Overall, the  $\delta^{56}$ Fe of partial melts produced in a system that undergoes melt extraction would only deviate from values for batch melting when biotite is completely exhausted, with estimated differences of less than 0.05 % (Fig. S6). Conversely, continuous aggregation of melt batches from successive MLEs forms hybrid melts that are more strongly influenced by isotopic composition of the earliest batches. As a result, aggregated melts generated at temperatures above biotite-out boundary tend to resemble the isotopically heavier melts produced during biotite dehydration melting (Fig. S6).

# 6.2.3. Oxygen fugacity

Oxygen fugacity is also expected to influence the extent of isotopic fractionation, having a strong control on the stability of iron-bearing phases and  ${\rm Fe}^{3+}/\Sigma{\rm Fe}$  ratios (Fig. 8c). For example, up to  ${\sim}15$  mol% garnet is produced during partial melting of SP-16-16 at 0.4 GPa at reducing conditions (i.e., FMQ-2 or FMQ oxygen fugacity), but under more oxidizing conditions (e.g., FMQ+2), approximately the same amount of magnetite would be produced instead of garnet (Figs. 6 and 7). Although such oxidizing conditions are unlikely to have existed during partial melting of the Zealand metasedimentary rocks, replacing garnet with magnetite would result in lower isotopic fractionation between the melt and the residue. Thus, granitic melts derived during partial melting of pelitic metasedimentary rocks under higher oxygen fugacity conditions are expected to be isotopically heavier than those formed at lower oxygen fugacity at low temperatures (<775 °C) and isotopically lighter at higher temperatures.

Differences in the iron isotope compositions of melts produced under different fO2 conditions can be resolvable with current analytical precision, particularly for granitic samples representing low melt fractions. However, retrieving redox conditions from Fe isotopes in natural granite samples would necessitate complementary information about the majorelement and isotopic composition of the protolith, as well as estimates of the melt fraction and metamorphic conditions at which the melt formed. It is also worth noting that overlapping regions in the iron isotope composition of melts produced at different oxygen fugacity may exist. For example, at  $\sim$ 750 °C or  $\sim$ 40 mol.% melt, the model for partial melting of the Zealand unit predicts nearly the same Fe isotope composition for all considered fO<sub>2</sub> conditions (Fig. 8b and 8d), rendering Fe isotopes ineffective as a redox indicator in such cases. Nevertheless, even under variable  $fO_2$  conditions, the predicted iron isotope compositions of SPGs and their complementary residual lithologies display smaller fractionation relative to their source than the large variability observed in the sedimentary record.

# 6.2.4. Pressure

Finally, the pressure conditions during metamorphism and anatexis can affect isotopic fractionation between the melt and the complementary residue (Fig. 8d). During the modeled melting behavior of SP-16-16, the stability field of biotite extends to higher temperatures at 0.4 GPa compared to 0.3 GPa as additional H2O is necessary to minimally saturate the system at the solidus (see Supplementary Fig. S2). As a result, biotite dehydration melting occurs over a wider temperature range and produces more extensive melting at 0.4 GPa ( $\sim$ 60 mol%) than at 0.3 GPa (~40 mol%). The difference in  $\Delta^{56}$ Fe<sub>melt-residue</sub> between the two pressures from the solidus to the temperature of biotite exhaustion at 0.3 GPa is minimal since partial melting in both cases is caused by  $\ensuremath{\text{H}_2\text{O}}$  released from biotite reacting with feldspar and quartz to produce melt + garnet (Spear, 1993). However, the amount of garnet produced during biotite dehydration controls the magnitude of  $\Delta^{56}$ Fe<sub>melt-residue</sub>. For example, in the FMQ-2 and FMQ models, isotopic fractionation at 0.4 GPa increases by  $\sim$ 0.18 % from  $\sim$ 750 °C to  $\sim$ 810 °C before biotite is completely consumed, as the melting reaction also produces a significant amount of garnet (Fig. 8d). At 0.3 GPa, only a small amount of garnet is produced, and  $\Delta^{56} Fe_{melt\text{-residue}}$  decreases nearly monotonically until biotite is exhausted (Fig. 8d). In general, garnet stability increases

with pressure, but it also depends on the major element composition of the system. With SP-16-16, a small proportion of garnet is stable at 0.3 GPa over a reduced temperature range; other more Al- or Mn-rich metapelite compositions, however, may stabilize more garnet at these pressure conditions, resulting in significant isotopic fractionation between the melt and the stable mineral assemblage.

In summary, the iron isotopic composition of SPGs is controlled by several factors during partial melting. Variations in mineral chemistry and metamorphic conditions lead to changes in the iron bonding environment, which translate into variable iron force constant values for the melt and residue phases. The initial H<sub>2</sub>O content controls the position of the solidus, as well as the melt fraction and composition. For all H<sub>2</sub>O contents, isotopic fractionation between the melt and the complementary solid is greatest near the solidus and decreases as the proportion of iron in the melt increases. However, regardless of the initial hydration state of the system, melts generated at the same temperature conditions are predicted to have similar  $\delta^{56}$ Fe<sub>melt</sub>. Furthermore, the stability of iron-bearing phases is strongly dependent on fO2 conditions, thus influencing the extent of isotopic fractionation. Partial melts produced under different fO2 conditions may be distinguished with current analytical precision if the protolith composition and metamorphic conditions are known. It is also possible for melts produced under different  $fO_2$  conditions to have identical  $\delta^{56}$ Fe<sub>melt</sub> compositions, in which case Fe isotopes cannot be used as redox proxies. Pressure conditions also play a role, affecting the stability and proportion of minerals like garnet and biotite, which in turn influence isotopic fractionation between the melt and the solid residue. The interplay of these variables results in granitic melts and restitic rocks that generally reflect the isotopic composition of their metasedimentary sources, with only minor fractionation relative to the source.

# 6.3. Equilibrium Fe isotope fractionation in the GLB

There is general agreement between the iron isotope composition of the granite samples and their mineralogy. Relatively high  $\delta^{56}$ Fe values ( $\sim+0.2-0.3$  %) correspond to samples in which biotite and accessory ilmenite are the main iron-bearing phases (Fig. 5). In contrast, the isotopic composition of SP-16-33, with the lowest  $\delta^{56}$ Fe among the granite samples (+0.111  $\pm$  0.018 %), is strongly influenced by abundant garnet and tourmaline in similar modal proportions. Although we did not measure individual garnet grains, garnet is expected to be isotopically light and can significantly lower the whole-rock isotopic composition when present in a large proportion (Fig. 5). Tourmaline in equilibrium with garnet is expected to have a higher  $\delta^{56}$ Fe (Nie et al., 2021), but its contribution to the whole-rock isotopic composition is less than that of garnet because it contains less iron (~13 wt% FeO in tourmaline versus ~36 wt% FeO in garnet for sample SP-16-33; Supplementary Table S3). The higher  $\delta^{56}$ Fe of sample SP-16-34, also containing garnet + tourmaline, can be explained by a larger proportion of biotite.

Equilibrium isotopic fractionation due to biotite dehydration melting can explain the, on average, higher  $\delta^{56}$ Fe of the GLB compared to the Zealand unit metasedimentary rocks (+0.192 ‰ versus +0.101 ‰, respectively). The predicted  $\Delta^{56}$ Fe<sub>melt-residue</sub> is at a maximum during the later stage of biotite dehydration melting for the FMQ and FMQ-2 oxygen buffers (~800-810 °C), reaching values of ~+0.300 ‰ and  $\sim +0.250$  ‰, respectively (Fig. 7). The shape of the  $\Delta^{56}$ Fe<sub>melt-residue</sub> model is almost identical to the  $\delta^{56} Fe_{melt}$ , as the transfer of iron to the melt is minor, and the iron fraction in the residue is considerably higher than in the melt (Figs. 7, 8d, and 9). Thus, biotite dehydration melting causes significant isotopic fractionation between the melt and the source (up to  $\sim$ 0.250–0.300 ‰), but negligible fractionation between the source and the residue (<0.012 ‰ at  $\sim\!800\text{--}810~^\circ\text{C}$  ). Thus, the restitic sample SP-16-30, with  $\delta^{56}\mbox{Fe}$  of 0 %, represents a reasonable estimate of the isotopic composition of the source for the GLB magmas, in addition to the metapelites from the Zealand unit.

Fig. 9 shows the predicted  $\delta^{56}$ Fe<sub>melt</sub> assuming the source to have the

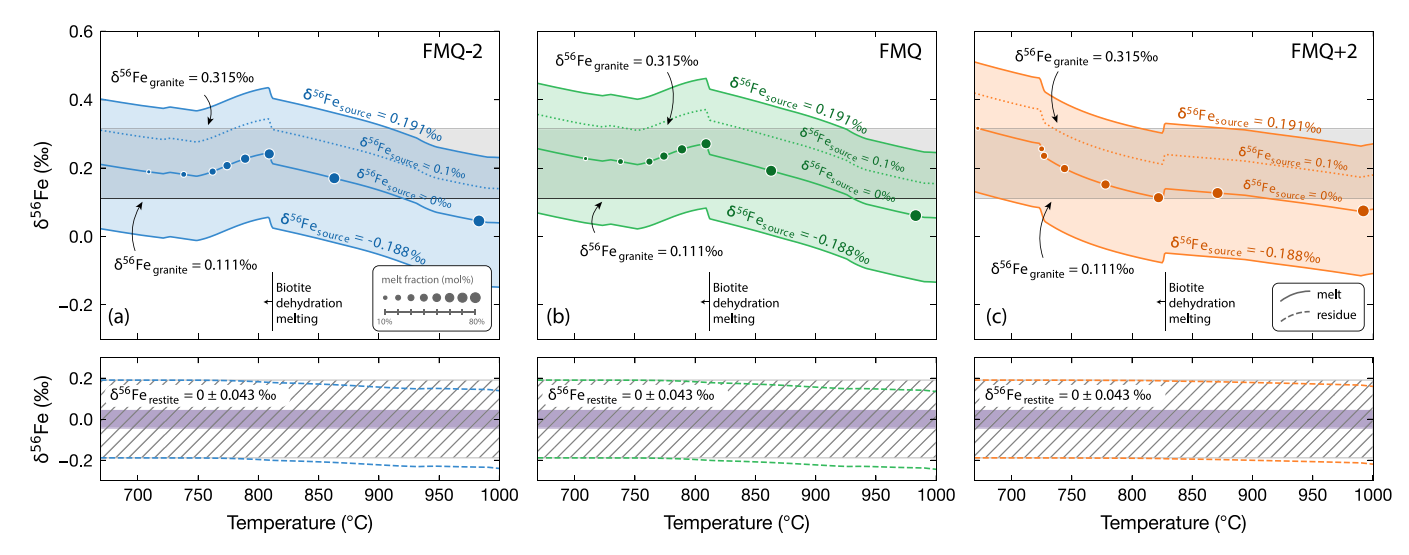


Fig. 9. Predicted iron isotope compositions for granitic SPG melts (top panels) and complementary residues (bottom panels) produced by partial melting of metapelite SP-16-16 at 0.4 GPa at variable oxygen fugacity conditions: (a) FMQ-2 (blue), (b) FMQ (green), and (c) FMQ+2 (orange). In the top panels, continuous lines are the predicted isotopic compositions with variable source compositions, whereas dotted lines are predicted melt iron isotope compositions with the mean  $\delta^{56}$ Fe of the Zealand unit metasedimentary rocks (0.1 ‰). The gray region is the range of measured isotopic compositions for the GLB. Circles with variable sizes represent melt fractions varying from 10 % to 80 % in increments of 10 %. In the bottom panels, the purple region is the isotopic composition of the restitic sample SP-16-30. Colored dashed lines mark the range of predicted isotopic compositions for the residual assemblages produced during partial melting with source  $\delta^{56}$ Fe compositions varying from -0.188 % to 0.191 % (the range measured in Zealand unit rocks). The hatched area is the range of isotopic compositions measured in the metapelite samples from the Zealand unit.

range of isotopic compositions observed in Zealand unit metasedimentary rocks (i.e.,  $\delta^{56}$ Fe from -0.188 to +0.191 %, averaging +0.1 %). The range of isotopic compositions measured in the granite samples varies between  $+0.111\pm0.018$  % and  $+0.315\pm0.038$  % (grey band in Fig. 9), which is a narrower range (0.204 %) than that defined by the metasedimentary samples (0.379 %), partly explained by isotopic homogenization during anatexis (see Section 6.4). Calculated  $\delta^{56}$ Fe<sub>melt</sub> values at the onset of melting (~680 °C) increase with increasing oxygen fugacity, reaching a peak at the onset of partial melting in all modeled redox conditions and also at the latter stages of biotite dehydration melting in the case of the FMO-2 and FMO oxygen buffers. Progressive lowering of  $\delta^{56}$ Fe<sub>melt</sub> values is expected for the FMQ+2 buffer during biotite dehydration melting as magnetite stabilizes instead of garnet. However, the absence of equilibrium assemblages containing magnetite or other highly oxidized species suggests that magma generation for the GLB occurred under more reduced conditions, as determined by previous work (maximum inferred oxygen fugacity of ~FMQ-1; Bucholz et al., 2018).

The range of  $\delta^{56} Fe$  measured in the granites is contained within the calculated  $\delta^{56} Fe_{melt}$  values for the FMQ-2 and FMQ models during biotite dehydration melting, using the range of observed compositions from the Zealand unit  $(-0.188\pm0.023~to~+0.191\pm0.035~\%)$  (Fig. 9). However, when considering the mean  $\delta^{56} Fe$  of the Zealand unit metasedimentary rocks as the source composition (+0.101 %), only the heaviest granite compositions (>+0.277 %) are predicted by the FMQ-2 model at temperatures <850 °C, whereas the FMQ model predicts higher  $\delta^{56} Fe_{melt}$  than the values measured in most the granite samples (>+0.310 %). Excluding the sulfide-rich metapelite SP-16-11 from the metasedimentary average and assuming the source composition is 0 %, the FMQ-2 model predicts most of the measured granite iron isotope compositions except for values < +0.177 %, whereas the FMQ model predicts the heaviest granite (>+0.210 %) compositions.

In summary, the iron isotope compositions of granite samples from the GLB reflect their mineral content. High  $\delta^{56}$ Fe values are associated with biotite and ilmenite, and the lowest to garnet and tourmaline-rich samples. Equilibrium iron isotope fractionation due to biotite dehydration melting at low oxygen fugacity (FMQ-2 and FMQ buffers) accounts for measured isotopic differences between the GLB and the Zealand unit

metapelites ( $\sim$ 0.12–0.30 %). This process also results in negligible fractionation between the source and the solid residue, consistent with previous studies on iron isotope fractionation between strongly peraluminous granites and their source (Telus et al., 2012; Xu et al., 2017; Nie et al., 2021). Thus, restitic lithologies, like sample SP-16-30, may closely approach the bulk composition for the source of SPG magmas.

Furthermore, most measured  $\delta^{56}$ Fe values in granite samples from the GLB can be explained by equilibrium isotope fractionation during biotite dehydration melting under reducing conditions, if the source has  $\delta^{56}$ Fe of 0 ‰. In contrast, the average  $\delta^{56}$ Fe measured in metapelite samples (+0.101 ‰) can only account for isotopically heavy granite samples. In general, the source composition dictates the equilibrium  $\delta^{56}$ Fe composition of granite samples. Thus, if equilibrium fractionation is the process that contributes the most to the iron isotope composition of SPGs, these rocks can be used to trace the composition of their sedimentary source.

# 6.4. Isotopic variability within the GLB

While the range of Fe isotope compositions in granite samples from the GLB is relatively narrow ( $\sim\!0.2$  %), equilibrium fractionation between SPG magmas and the average composition of their source can only account for  $\delta^{56}$ Fe values greater than +0.177 %. In this section, we explore the roles of assimilation, magmatic differentiation, and fluid exsolution, processes that are likely to occur during anatexis and batholith emplacement. Specifically, we discuss whether these processes could impart the magmas from which the GLB crystallized with an isotopic composition that is lighter than what equilibrium fractionation models predict.

The amount of restitic or source/host rocks required to be mixed in the melt to explain the lowest  $\delta^{56} Fe$  values measured in the granite depends on the composition of the source. For example, using the FMQ-2 model at  $\sim\!770~^\circ\text{C}$  with a source  $\delta^{56} Fe = +0.1~\%$  and FeO =5 wt%, the calculated  $\delta^{56} Fe_{melt}$  is  $\sim\!+0.3~\%$  with a FeO content of  $\sim\!1$  wt%. Assimilation of  $\sim\!20\!-\!80~\%$  by mass of source or restitic rocks is needed to produce melt compositions with  $\delta^{56} Fe$  between +0.1 and +0.2~%. By contrast, assuming a source  $\delta^{56} Fe = 0~\%$ , the  $\delta^{56} Fe$  of the melt is  $\sim\!+0.2~\%$  at  $\sim\!770~^\circ\text{C}$ , which would require less than 15 % of source rock or

restite to produce the lowest granite compositions measured. It is also possible for the melt to assimilate peritectic phases such as garnet. For instance, if a melt containing  $1\,\%$  FeO and  $\delta^{56}\text{Fe}=+0.3\,\%$  absorbs  $\sim\!5\,\%$  by mass of an almandine-rich garnet composition with 30 % FeO and  $\delta^{56}\text{Fe}=0$ %, the  $\delta^{56}\text{Fe}$  of the melt would decrease to +0.12%. No correlation between  $\delta^{56}\text{Fe}$  and FeO is observed, however, so peritectic garnet entrainment is likely not the dominant control on the  $\delta^{56}\text{Fe}$  in the granites.

During partial melting, assimilation of source rock material can also result in dissolution of sulfides in the melt as FeS species (Clémente et al., 2004; Klimm et al., 2012; Bucholz et al., 2020). Less than 1 % of isotopically light pyrrhotite like that in SP-16-11 would need to be dissolved in the melt to produce the lowest  $\delta^{56}$ Fe measured in granite samples. However, pyrrhotite in the Zealand unit metasedimentary rocks has variable isotopic composition, with  $\delta^{56}$ Fe ranging from -0.337 to +0.364 % (Fig. 5), and assimilation of isotopically heavy sulfides could also increase the melt  $\delta^{56}$ Fe. An example of this process could be the sample SP-16-22, which has the highest  $\delta^{56}$ Fe composition among the measured granite samples. Evidence of sulfide dissolution in this sample comes from sulfur isotopes showing incomplete reequilibration between the melt phase and fluid H<sub>2</sub>S from pyrite breakdown during assimilation of the metasedimentary host rock (Bucholz et al., 2020).

An alternative model for the isotopic variability observed in the GLB is related to the internal differentiation of the magmatic pluton. Granitic plutons can be understood as variable mixtures of magmatic liquids and cumulus material produced by magmatic crystallization (Bea et al., 1994; Chappell and Wyborn, 2004; Chappell and Hine, 2006). During differentiation, the melt component is expected to have a heavier iron isotope composition than the cumulate counterpart due to its higher  ${\rm Fe}^{+3}/{\rm \Sigma}{\rm Fe}$  and  ${\rm SiO}_2$  content. If a granite sample represents a large melt-to-cumulate ratio, its iron isotope composition would be heavier than a sample with a lower melt component. A simple Rayleigh fractionation model illustrates this scenario (Fig. 10). Let us consider a crystallizing liquid produced at  $\sim$ 800 °C during partial melting of SP-16-16 at FMQ-

2. The liquid composition is multiply saturated with the phases in the residual assemblage and will thus start to crystallize the same assemblage with a  $\Delta^{56}$ Fe<sub>melt-cumulate</sub> of ~0.2 % (same as  $\Delta^{56}$ Fe<sub>melt-residue</sub>). The melt and crystallizing assemblage become isotopically heavier as fractional crystallization progresses, but the melt is always heavier. If the cumulate produced after crystallization of the initial 20 % iron fraction  $(\delta^{56} Fe = +0.04 \%)$  is arbitrarily mixed with the liquid containing 40 % of the original iron fraction ( $\delta^{56}$ Fe = +0.38 %) in a melt-to-cumulate ratio of 1:4, the resulting granite  $\delta^{56}$ Fe will be +0.112 ‰. Local variability in melt segregation may allow mixing of variable melt-tocumulate proportions in addition to mixing of melts and cumulates produced at different iron fractions. Therefore, the range of iron isotope compositions measured in the granite samples from the GLB can be attributed to variable melt-cumulus proportions. In this model, the average of the metapelites can produce melts with heavier iron isotope compositions due to equilibrium fractionation. Subsequent partial crystallization and incomplete magma segregation would produce variable proportions of the cumulate versus melt in the solidified granite.

Hydrothermal fluids exsolved during magma crystallization can transport significant amounts of metals, forming economic ore deposits (Richards, 2011; Audétat, 2019). This process can cause iron isotopic fractionation as the exsolving fluids can remove sufficient iron with a particular isotopic composition to alter that of the original magma (e.g., Wawryk and Foden, 2015; Wang et al., 2021). The extent of isotopic fractionation depends on the fraction of fluid exsolved from the melt during crystallization and the iron content of that fluid. The amount of fluid released is determined by fluid solubility in the magma at specific P-T conditions, and whether the fluid is released as a free phase or incorporated into crystallizing hydrous phases. Our phase equilibrium calculations yield melt compositions with  $\sim$ 6-8 wt% dissolved H<sub>2</sub>O, consistent with common estimates for silicic magmas (Clemens, 1984). On the other hand, the proportion of iron in the fluid is controlled by the partitioning of iron between the fluid and the magma, which may depend on factors such as the salinity of the fluid, the magma composition, and the depth of exsolution (Simon et al., 2004; Zajacz et al.,

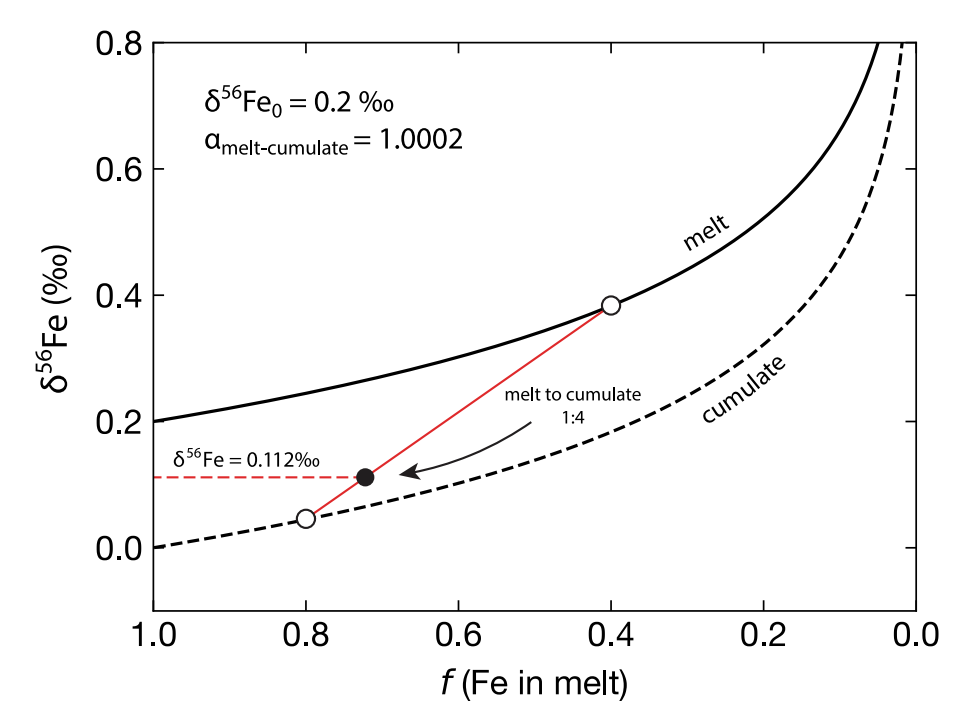


Fig. 10. Rayleigh fractionation model illustrating fractional crystallization of a melt (continuous line) and corresponding cumulus assemblage (dashed line) as the fraction of iron decreases with decreasing temperature. The initial melt has a  $\delta^{56}$ Fe = 0.2 ‰, similar to that produced at 800 °C with the FMQ-2 model. The fractionation factor between the melt and the crystallizing assemblage ( $\Delta^{56}$ Fe melt-cumulate) is assumed to be 0.2 ‰ ( $\alpha_{melt-cumulate} = 1.0002$ ). The white dots represent, respectively, an arbitrary melt when the remaining iron fraction is 0.4 and a cumulus assemblage produced when the iron fraction in the melt was 0.8. Mixing 20 % melt with 80 % cumulate results in a granite isotopic composition of  $\delta^{56}$ Fe = 0.112 ‰.

2008). The partition coefficients between magmatic-hydrothermal fluids and melt (D<sup>fluid/melt</sup>) can vary by one to two orders of magnitude, with a strong dependence on the chlorine content of the fluid (Zajacz et al., 2008; Audétat, 2019). Accordingly, Fe contents in magmatic fluids can range from less than 1 wt% up to ~5 wt% (e.g., Audétat and Pettke, 2003; Zajacz et al., 2008; Bartoli et al., 2013; Audétat, 2019). To decrease  $\delta^{56}$ Fe<sub>melt</sub>, however, the fluid must be isotopically heavier than the crystallizing magma, which contradicts  $\Delta^{56}$ Fe<sub>fluid-melt</sub> estimations for chlorine-bearing fluids in equilibrium with magmas produced by partial melting of the GLB protolith (see Supplementary Material). Thus, fluid exsolution may not have significantly impacted the isotopic composition of granite samples from the GLB. However, this process may still be important for the iron isotope composition of other granites (Poitrasson and Freydier, 2005; Heimann et al., 2008), including SPGs where large amounts of iron-rich fluids have been exsolved (e.g., Wawryk and Foden, 2015).

In summary, assimilation of source/host rock or sulfides with lighter iron isotope composition could drive the composition of isotopically heavy partial melts to lower  $\delta^{56}\text{Fe}$  values. However, no correlation exists between  $\delta^{56}\text{Fe}$  values and  $\text{FeO}_T$  in the GLB samples (see Supplementary Fig. S4), indicating that entrainment and assimilation of restites, host lithologies, peritectic phases, or sulfides probably did not significantly contribute to most granite iron isotope compositions. Alternatively, the iron isotope variability in granite samples could be attributed to variable proportions of granitic melt and cumulate minerals (such as biotite, garnet, and Fe-Ti oxides). In this case, granite samples with low  $\delta^{56}\text{Fe}$  values would be indicative of lower melt-to-cumulus ratios, whereas isotopically heavier granites may be closer to crystallized liquids, with iron isotope compositions mainly controlled by equilibrium fractionation.

# 6.5. Implications for iron isotopes in SPGs and their relationship with the sedimentary record

Although the results we present here are specific to the GLB, the implications extend to most SPGs. Metamorphism and partial melting can both cause iron isotope fractionation between SPGs and their sedimentary sources. The influence of metamorphism, however, is expected to be minimal, as progressive fluid loss from the protolith during metamorphism may not significantly modify its composition. Moreover, prograde metamorphism is expected to partially redistribute iron isotopes among stable phases, minimizing inter-mineral heterogeneities without significantly affecting the bulk isotopic composition of the protolith. Consequently, the iron isotope composition of SPG protoliths should closely resemble the average composition of the original sedimentary rock before metamorphism.

Most isotopic fractionation occurs during partial melting, resulting in relatively small isotopic differences between SPGs and their sources. The magnitude of this equilibrium fractionation depends on several interdependent factors, including the composition of the phases involved in partial melting reactions, P-T conditions, and the oxidation state of the system. For reduced sedimentary sources typical of most SPGs, maximum isotopic fractionation may occur at two distinct points: the earliest stages of partial melting, close to the wet granite solidus, or at temperatures close to near-complete biotite dehydration melting. The former could be related to some anatectic migmatites, while the latter could be more likely recorded in larger granitic bodies like SPG batholiths, most often formed through fluid-absent melting reactions (Stevens and Clemens, 1993; Clemens and Watkins, 2001; Clemens, 2003; Clemens et al., 2020). It is noteworthy that the magnitude and direction of isotopic fractionation between SPGs and their source is controlled by the conditions at which partial melting occurs, which are likely specific to each locality. However, the extent of equilibrium fractionation is expected to remain within a few tenths of a permil for most SPGs, as the major element compositions of sedimentary protoliths and derived partial melt compositions are relatively uniform over time and space

(Sylvester, 1998; Clemens, 2003; Nabelek, 2020; Bucholz and Spencer, 2019).

Additional processes during batholith emplacement and magma crystallization can also influence the isotopic composition of partial melts. These include assimilation of isotopically lighter lithologies and minerals from the source or host rock, entrainment of iron-bearing peritectic phases like garnet, and exsolution of chlorine-rich fluids enriched in Fe. Moreover, granite rocks can consist of mixtures of crystallized liquid and cumulus minerals, each with distinct isotopic compositions. Variable proportions of these components in granite samples will lead to variations in their iron isotope composition. Notably, while these processes can modify the iron isotope composition of SPGs, the deviations from equilibrium fractionation are expected to be minor.

Importantly, SPGs not only inherit isotopic compositions close to that of their source but also display a significantly smaller range of variation in iron isotope compositions compared to sedimentary rocks. For example, while the Archean and Proterozoic bulk-rock sedimentary record exhibits a dispersion exceeding 2 ‰, variability in SPGs is only  $\sim\!0.2\,\%$  (Fig. 11). Even within individual sedimentary formations, bulk-rock samples can exhibit  $\delta^{56}$ Fe variability >1 ‰ (e.g., Yamaguchi et al., 2005; Johnson et al., 2008; Bekker et al., 2010; Fabre et al., 2011; Busigny et al., 2014; Heard et al., 2020; Ostrander et al., 2022). The smaller range of variability in SPGs likely results from isotopic homogenization of the partially melted protolith during anatexis and the dominant source of Fe being derived from detrital minerals in the protolith (rather than chemical). Therefore, SPGs can serve as a reliable archive of the iron isotope evolution in the bulk siliciclastic sedimentary record.

#### 7. Conclusions

Fe isotope fractionation between SPGs and their metasedimentary source results from a complex interplay between metamorphic and magmatic processes during anatexis. Equilibrium isotopic fractionation during partial melting is primarily controlled by the iron isotope composition of the protolith, which can be diverse even within the same unit. Metamorphism may cause only minimal isotopic fractionation so that the protolith likely reflects the isotopic signature of the sedimentary source. However, inter-mineral fractionation can persist or develop at high metamorphic grades.

As partial melting progresses, the equilibrium mineral assemblage controls the Fe isotope composition of the melt. Both mineral stability and phase compositions change in response to variations in the P-T conditions of the system and are strongly dependent on fO2. It is commonly assumed that higher temperatures lead to lower isotopic fractionation between phases at equilibrium, such as melt and restitic phases. However, temperature changes can stabilize phases with a different iron bonding environment and alter the average force constant, [F], of the solid phases, thereby varying the extent of isotopic fractionation between the melt and the residual assemblage. Similarly, variations in pressure can affect the stability field of phases like garnet at a given temperature, which can impact the extent of isotopic fractionation between the melt and the residue. Significant differences in iron isotope fractionation are also expected between melts produced under contrasting fO2 conditions. For reduced metasedimentary sources, typical of those inferred for the generation of SPG magmas, the maximum isotopic fractionation between the melt and the residue is predicted at low melt fractions and at temperatures approaching nearcomplete biotite dehydration melting.

Since anatexis can homogenize the isotopic composition of the sedimentary protolith, the average source composition determines the iron isotope composition of partial melting products. Isotopic differences between SPGs and their source can be attributed to equilibrium fractionation during biotite dehydration melting, while restitic lithologies exhibit almost no fractionation from the source. Other processes

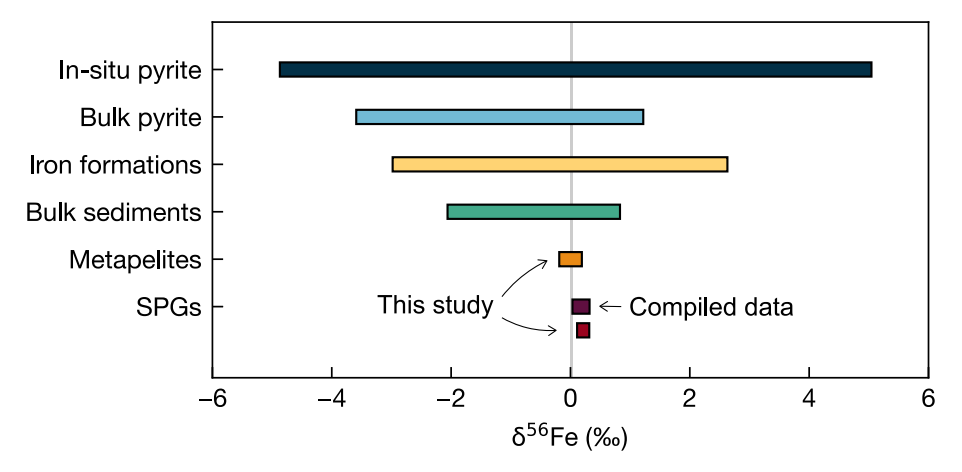


Fig. 11. Variations in  $\delta^{56}$ Fe for lithologies representative of the Archean-Proterozoic sedimentary record from the same dataset as in Fig. 1a. Significantly less isotopic variability exists in metapelites and SPGs. Compiled data for SPGs includes our results and compositions from Telus et al. (2012) and Foden et al. (2015). The gray vertical line is the mantle composition (Craddock et al., 2013).

occurring during anatexis and magma emplacement may cause isotopic variability in SPG magmas. These processes, however, have only a minor contribution to the iron isotope composition of SPGs relative to equilibrium fractionation. Therefore, SPGs and associated restitic rocks can provide a reliable record of the iron isotope evolution in sedimentary rocks. This is further evidenced by the small range of variability in SPGs compared to the broader sedimentary record.

In sum, the Fe isotope composition of SPGs is controlled by the isotopic composition of their sedimentary protolith. While it is essential to consider other factors, such as P-T and  $fO_2$  conditions during melt generation, as well as processes during magma segregation and granite emplacement, the extent of iron isotope fractionation they introduced is minimal when compared to broader isotopic variations in the sedimentary record. The Fe isotope variability in SPGs is  $\sim$ 0.2 ‰, significantly smaller than variations exceeding 2 ‰ found in the sedimentary record (Fig. 11). Hence, SPGs can represent a reliable proxy to track changes in the iron isotope composition of siliciclastic sedimentary rocks over time (Fig. 1a).

# Data availability

Data are available through Mendeley Data at https://doi.org/10.17632/4msrjttgcm.2.

#### CRediT authorship contribution statement

Juan David Hernández-Montenegro: Writing – review & editing, Writing – original draft, Visualization, Methodology, Formal analysis, Conceptualization. Claire E. Bucholz: Writing – review & editing, Writing – original draft, Visualization, Validation, Supervision, Methodology, Funding acquisition, Formal analysis, Conceptualization. Emma S. Sosa: Writing – review & editing, Writing – original draft, Validation, Methodology. Michael A. Kipp: Writing – review & editing, Resources, Methodology. François L.H. Tissot: Writing – review & editing, Supervision, Resources, Funding acquisition, Formal analysis.

# Declaration of competing interest

The authors declare that they have no known competing financial interests or personal relationships that could have appeared to influence the work reported in this paper.

# Acknowledgments

We thank Paul Asimow, Nicole Nie, and Shane Houchin for insightful

discussions on iron isotopes and petrological modeling. We also thank Gerrit Budde, Rosa Grigoryan, and Ren Marquez for their assistance with sample preparation and isotopic analysis. Juan David Hernández-Montenegro acknowledges support from a Fulbright Foundation grant. Claire Bucholz thanks Fred Breaks for introducing her to the Ghost Lake batholith. This work was supported by NSF grant EAR-1943629 awarded to C. Bucholz. We appreciate the constructive comments from Paul Savage and two anonymous reviewers, which significantly improved this manuscript. We are also grateful to Stefan Weyer for editorial handling.

#### Appendix A. Supplementary material

This supplementary material presents additional information on iron isotope fractionation during partial melting of metapelites and the generation of SPGs, including: 1) the effects of variable hydration states on the Fe isotope composition of melts; 2) the influence of melt loss on the Fe isotope composition of melts and residues; 3) the Fe isotope fractionation between fluid and melt during fluid exsolution; 4) additional figures showing the Fe isotope composition of SPG and metasedimentary samples versus whole-rock chemistry; and 5) tables containing whole-rock geochemistry and petrographic observations for all samples. Supplementary material to this article can be found online at https://doi.org/10.1016/j.gca.2024.07.016.

# References

Agangi, A., Hofmann, A., Rollion-Bard, C., Marin-Carbonne, J., Cavalazzi, B., Large, R.,
 Meffre, S., 2015. Gold accumulation in the Archaean Witwatersrand Basin, South
 Africa — evidence from concentrically laminated pyrite. Earth Sci. Rev. 140, 27–53.
 Ague, J.J., 1991. Evidence for major mass transfer and volume strain during regional
 metamorphism of pelites. Geology 19, 855.

Ague, J.J., 2014. 4.6 - Fluid flow in the deep crust. In: Holland, H.D., Turekian, K.K. (Eds.), Treatise on Geochemistry, second edition. Elsevier, Oxford, pp. 203–247.
 Anbar, A.D., Rouxel, O., 2007. Metal stable isotopes in paleoceanography. Annu. Rev. Earth Planet. Sci. 35, 717–746.

Archer, C., Vance, D., 2006. Coupled Fe and S isotope evidence for Archean microbial Fe (III) and sulfate reduction. Geology 34, 153–156.

Audétat, A., 2019. The metal content of magmatic-hydrothermal fluids and its relationship to mineralization potential. Econ. Geol. 114, 1033–1056.

Audétat, A., Pettke, T., 2003. The magmatic-hydrothermal evolution of two barren granites: a melt and fluid inclusion study of the Rito del Medio and Canada Pinabete plutons in northern New Mexico (USA). Geochim. Cosmochim. Acta 67, 97–121.

Azimov, P.Y., Bushmin, S.A., 2007. Solubility of minerals of metamorphic and metasomatic rocks in hydrothermal solutions of varying acidity: thermodynamic modeling at 400–800°C and 1–5 kbar. Geochem. Int. 45, 1210–1234.

Bartoli, O., Cesare, B., Poli, S., Bodnar, R.J., Acosta-Vigil, A., Frezzotti, M.L., Meli, S., 2013. Recovering the composition of melt and the fluid regime at the onset of crustal anatexis and S-type granite formation. Geology 41, 115–118.

- Bea, F., Pereira, M.D., Corretgé, L.G., Fershtater, G.B., 1994. Differentiation of strongly peraluminous, perphosphorus granites: the pedrobernardo pluton, central Spain. Geochim. Cosmochim. Acta 58, 2609–2627.
- Beard, B.L., Johnson, C.M., 2004. Fe isotope variations in the modern and ancient earth and other planetary bodies. Rev. Mineral. Geochem. 55, 319–357.
- Bekker, A., Slack, J.F., Planavsky, N., Krapež, B., Hofmann, A., Konhauser, K.O., Rouxel, O.J., 2010. Iron formation: the sedimentary product of a complex interplay among mantle, tectonic, oceanic, and biospheric processes\*. Econ. Geol. 105, 467-508
- Bigeleisen, J., Mayer, M.G., 1947. Calculation of equilibrium constants for isotopic exchange reactions. J. Chem. Phys. 15, 261–267.
- Blackburn, C., Johns, G., Ayer, J., Davis, D., 1991. Wabigoon subprovince. Geol. Ont. 4, 303–381.
- Borisov, A., Behrens, H., Holtz, F., 2015. Effects of melt composition on Fe<sup>3+</sup>/Fe<sup>2+</sup> in silicate melts: a step to model ferric/ferrous ratio in multicomponent systems. Contrib. Miner. Petrol. 169, 24.
- Breaks, F.W., Moore, J.M., 1992. The Ghost Lake Batholith, Superior Province of northwestern Ontario; a fertile, S-type, peraluminous granite-rare-element pegmatite system. Can. Mineral. 30, 835–875.
- Bucholz, C.E., 2022. Coevolution of sedimentary and strongly peraluminous granite phosphorus records. Earth Planet. Sci. Lett. 596, 117795.
- Bucholz, C.E., Biasi, J.A., Beaudry, P., Ono, S., 2020. Sulfur isotope behavior during metamorphism and anatexis of Archean sedimentary rocks: a case study from the Ghost Lake batholith, Ontario Canada. Earth Planet. Sci. Lett. 549, 116494.
- Bucholz, C.E., Spencer, C.J., 2019. Strongly peraluminous granites across the Archean-Proterozoic transition. J. Petrol. 60, 1299–1348.
- Bucholz, C.E., Stolper, E.M., Eiler, J.M., Breaks, F.W., 2018. A comparison of oxygen fugacities of strongly peraluminous granites across the Archean-Proterozoic boundary. J. Petrol. 59, 2123–2156.
- Bucholz, C.E., 2024. The diversity and origin of granites. In: Anbar, A., Weis, D. (Eds.), Treatise in Geochemistry. Elsevier.
- Busigny, V., Planavsky, N.J., Jézéquel, D., Crowe, S., Louvat, P., Moureau, J., Viollier, E., Lyons, T.W., 2014. Iron isotopes in an Archean ocean analogue. Geochim. Cosmochim. Acta 133, 443–462.
- Chappell, B.W., Hine, R., 2006. The cornubian batholith: an example of magmatic fractionation on a crustal scale. Resour. Geol. 56, 203–244.
- Chappell, B.W., White, A.J.R., 1992. I- and S-type granites in the Lachlan Fold Belt. Earth Environ. Sci. Trans. R. Soc. Edinb. 83, 1–26.
- Chappell, B.W., Wyborn, D., 2004. Cumulate and cumulative granites and associated rocks. Resour. Geol. 54, 227–240.
- Clarke, D.B., 2019. The origins of strongly peraluminous granitoid rocks. Can. Mineral. 57, 529–550.
- Clemens, J.D., 1984. Water contents of silicic to intermediate magmas. Lithos 17, 273–287.
- Clemens, J.D., 2003. S-type granitic magmas—petrogenetic issues, models and evidence. Earth-Sci. Rev. 61, 1–18.
- Clemens, J.D., Stevens, G., Bryan, S.E., 2020. Conditions during the formation of granitic magmas by crustal melting Hot or cold; drenched, damp or dry? Earth-Sci. Rev. 200. 102982.
- Clemens, J., Watkins, J., 2001. The fluid regime of high-temperature metamorphism during granitoid magma genesis. Contrib. Mineral. Petrol. 140, 600–606.
- Clémente, B., Scaillet, B., Pichavant, M., 2004. The solubility of sulphur in hydrous rhyolitic melts. J. Petrol. 45, 2171–2196.
- Craddock, P.R., Dauphas, N., 2011. Iron isotopic compositions of geological reference materials and chondrites. Geostand. Geoanal. Res. 35, 101–123.
- Craddock, P.R., Warren, J.M., Dauphas, N., 2013. Abyssal peridotites reveal the nearchondritic Fe isotopic composition of the Earth. Earth Planet. Sci. Lett. 63–76.
- Craig, J.R., Vokes, F.M., 1993. The metamorphism of pyrite and pyritic ores: an overview. Mineral. Mag. 57, 3–18.
- Dauphas, N., Janney, P.E., Mendybaev, R.A., Wadhwa, M., Richter, F.M., Davis, A.M., Van Zuilen, M., Hines, R., Foley, C.N., 2004. Chromatographic separation and multicollection-ICPMS analysis of iron. Investigating mass-dependent andindependent isotope effects. Anal. Chem. 76, 5855–5863.
- Dauphas, N., Cates, N.L., Mojzsis, S.J., Busigny, V., 2007a. Identification of chemical sedimentary protoliths using iron isotopes in the >3750 Ma Nuvvuagittuq supracrustal belt, Canada. Earth Planet. Sci. Lett. 254, 358–376.
- Dauphas, N., van Zuilen, M., Busigny, V., Lepland, A., Wadhwa, M., Janney, P.E., 2007b. Iron isotope, major and trace element characterization of early Archean supracrustal rocks from SW Greenland: protolith identification and metamorphic overprint. Geochim. Cosmochim. Acta 71, 4745–4770.
- Dauphas, N., Pourmand, A., Teng, F.-Z., 2009. Routine isotopic analysis of iron by HR-MC-ICPMS: how precise and how accurate? Chem. Geol. 267, 175–184.
- Dauphas, N., Roskosz, M., Alp, E.E., Golden, D.C., Sio, C.K., Tissot, F.L.H., Hu, M.Y., Zhao, J., Gao, L., Morris, R.V., 2012. A general moment NRIXS approach to the determination of equilibrium Fe isotopic fractionation factors: Application to goethite and jarosite. Geochim. et Cosmochim. Acta 94, 254–275.
- Dauphas, N., Roskosz, M., Alp, E.E., Neuville, D.R., Hu, M.Y., Sio, C.K., Tissot, F.L.H., Zhao, J., Tissandier, L., Médard, E., Cordier, C., 2014. Magma redox and structural controls on iron isotope variations in Earth's mantle and crust. Earth Planet. Sci. Lett. 398, 127–140.
- Dauphas, N., John, S.G., Rouxel, O., 2017. Iron isotope systematics. Rev. Mineral. Geochem. 82, 415–510.
- Davis, D.W., Sutcliffe, R.H., Trowell, N.F., 1988. Geochronological constraints on the tectonic evolution of a late Archaean greenstone belt, Wabigoon Subprovince, Northwest Ontario, Canada. Precambr. Res. 39, 171–191.

- Dupeyron, J., Decraene, M.-N., Marin-Carbonne, J., Busigny, V., 2023. Formation pathways of Precambrian sedimentary pyrite: insights from in situ Fe isotopes. Earth Planet. Sci. Lett. 609, 118070.
- Fabre, S., Nédélec, A., Poitrasson, F., Strauss, H., Thomazo, C., Nogueira, A., 2011. Iron and sulphur isotopes from the Carajás mining province (Pará, Brazil): implications for the oxidation of the ocean and the atmosphere across the Archaean-Proterozoic transition. Chem. Geol. 289, 124–139.
- Ferry, J.M., 1981. Petrology of graphitic sulfide-rich schists from South-central Maine: an example of desulfidation during prograde regional metamorphism. Am. Mineral. 66, 908–930.
- Foden, J., Sossi, P.A., Wawryk, C.M., 2015. Fe isotopes and the contrasting petrogenesis of A-, I- and S-type granite. Lithos 212–215, 32–44.
- Foden, J., Sossi, P.A., Nebel, O., 2018. Controls on the iron isotopic composition of global arc magmas. Earth Planet. Sci. Lett. 494, 190–201.
- Forshaw, J.B., Pattison, D.R.M., 2022. Major-element geochemistry of pelites. Geology 51, 39–43.
- Frost, B.R., Barnes, C.G., Collins, W.J., Arculus, R.J., Ellis, D.J., Frost, C.D., 2001. A geochemical classification for granitic rocks. J. Petrol. 42, 2033–2048.
- Frost, C.D., von Blanckenburg, F., Schoenberg, R., Frost, B.R., Swapp, S.M., 2007. Preservation of Fe isotope heterogeneities during diagenesis and metamorphism of banded iron formation. Contrib. Miner. Petrol. 153, 211–235.
- Galić, A., Mason, P.R., Mogollón, J.M., Wolthers, M., Vroon, P.Z., Whitehouse, M.J., 2017. Pyrite in a sulfate-poor Paleoarchean basin was derived predominantly from elemental sulfur: evidence from 3.2 Ga sediments in the Barberton Greenstone Belt, Kaapvaal Craton. Chem. Geol. 449, 135–146.
- Guidotti, C.V., Dyar, M.D., 1991. Ferric iron in metamorphic biotite and its petrologic and crystallochemical implications. Am. Mineral. 76, 161–175.
- Guiraud, M., Powell, R., Rebay, G., 2001. H<sub>2</sub>O in metamorphism and unexpected behaviour in the preservation of metamorphic mineral assemblages. J. Metam. Geol. 19, 445–454.
- He, Y., Wu, H., Ke, S., Liu, S.-A., Wang, Q., 2017. Iron isotopic compositions of adaktic and non-adaktic granitic magmas: magma compositional control and subtle residual garnet effect. Geochim. Cosmochim. Acta 203, 89–102.
- Heard, A., Dauphas, N., 2019. Archean-Paleoproterozoic pyrite and iron formation Fe isotope and sedimentary S isotope records.
- Heard, A.W., Dauphas, N., 2020. Constraints on the coevolution of oxic and sulfidic ocean iron sinks from archean-paleoproterozoic iron isotope records. Geology 48, 358–362.
- Heard, A.W., Dauphas, N., Guilbaud, R., Rouxel, O.J., Butler, I.B., Nie, N.X., Bekker, A., 2020. Triple iron isotope constraints on the role of ocean iron sinks in early atmospheric oxygenation. Science 370, 446–449.
- Heimann, A., Beard, B.L., Johnson, C.M., 2008. The role of volatile exsolution and subsolidus fluid/rock interactions in producing high <sup>56</sup>Fe/<sup>54</sup>Fe ratios in siliceous igneous rocks. Geochim. Cosmochim. Acta 72, 4379–4396.
- Hermann, J., Zheng, Y.-F., Rubatto, D., 2013. Deep fluids in subducted continental crust. Elements 9, 281–287.
- Hofmann, A., Bekker, A., Rouxel, O., Rumble, D., Master, S., 2009. Multiple sulphur and iron isotope composition of detrital pyrite in Archaean sedimentary rocks: a new tool for provenance analysis. Earth Planet. Sci. Lett. 286, 436–445.
- Holland, T., Powell, R., 2003. Activity-composition relations for phases in petrological calculations: an asymmetric multicomponent formulation. Contrib. Miner. Petrol. 145, 492–501.
- Holland, T.J.B., Powell, R., 2011. An improved and extended internally consistent thermodynamic dataset for phases of petrological interest, involving a new equation of state for solids. J. Metam. Geol. 29, 333–383.
- Hyslop, E.V., Valley, J.W., Johnson, C.M., Beard, B.L., 2008. The effects of metamorphism on O and Fe isotope compositions in the Biwabik Iron Formation, northern Minnesota. Contrib. Miner. Petrol. 155, 313–328.
- Johnson, C.M., Beard, B.L., Beukes, N.J., Klein, C., O'Leary, J.M., 2003. Ancient geochemical cycling in the Earth as inferred from Fe isotope studies of banded iron formations from the Transvaal Craton. Contrib. Miner. Petrol. 144, 523–547.
- Johnson, C.M., Beard, B.L., Roden, E.E., Newman, D.K., Nealson, K.H., 2004. Isotopic constraints on biogeochemical cycling of Fe. Rev. Mineral. Geochem. 55, 359–408.
- Johnson, C.M., Beard, B.L., Klein, C., Beukes, N.J., Roden, E.E., 2008. Iron isotopes constrain biologic and abiologic processes in banded iron formation genesis. Geochim. Cosmochim. Acta 72, 151–169.
- Khomenko, V.M., Langer, K., Geiger, C.A., 2001. Structural locations of the iron ions in cordierite: a spectroscopic study. Contrib. Miner. Petrol. 141, 381–396.
- Klimm, K., Kohn, S.C., Botcharnikov, R.E., 2012. The dissolution mechanism of sulphur in hydrous silicate melts. II: Solubility and speciation of sulphur in hydrous silicate melts as a function of fO<sub>2</sub>. Chem. Geol. 322–323, 250–267.
- Kress, V.C., Carmichael, I.S.E., 1991. The compressibility of silicate liquids containing  $Fe_2O_3$  and the effect of composition, temperature, oxygen fugacity and pressure on their redox states. Contrib. Miner. Petrol. 108, 82–92.
- Le Breton, N., Thompson, A.B., 1988. Fluid-absent (dehydration) melting of biotite in metapelites in the early stages of crustal anatexis. Contrib. Miner. Petrol. 99, 226–237.
- Lewis, M.J., Bucholz, C.E., Jagoutz, O.E., 2021. Evidence for polybaric fractional crystallization in a continental arc: Hidden Lakes mafic complex, Sierra Nevada batholith, California. Contrib. Mineral. Petrol. 176, 90.
- Liang, W., Huang, J., Zhang, G., Huang, F., 2022. Iron isotopic fractionation during eclogite anatexis and adakitic melt evolution: insights into garnet effect on Fe isotopic variations in high-silica igneous rocks. Contrib. Miner. Petrol. 177, 33.
- Liebmann, J., Spencer, C.J., Kirkland, C.L., Bucholz, C.E., Xia, X.-P., Martin, L., Kitchen, N., Shumlyanskyy, L., 2021. Coupling sulfur and oxygen isotope ratios in

- sediment melts across the Archean-Proterozoic transition. Geochim. Cosmochim. Acta 307, 242-257.
- Liou, P., Wang, Z., Mitchell, R.N., Doucet, L.S., Li, M., Guo, J., Zhai, M., 2022. Fe isotopic evidence that "high pressure" TTGs formed at low pressure. Earth Planet. Sci. Lett. 592, 117645.
- Ma, H.-Z., Chen, Y.-X., Zhou, K., Gao, P., Zheng, Y.-F., Zha, X.-P., Xia, X.-P., Zhao, Z.-F., Huang, F., 2022. The effect of crystal fractionation on the geochemical composition of syn-exhumation magmas: implication for the formation of high δ<sup>56</sup>Fe granites in collisional orogens. Geochim. Cosmochim. Acta 332, 156–185.
- Marin-Carbonne, J., Rollion-Bard, C., Bekker, A., Rouxel, O., Agangi, A., Cavalazzi, B., Wohlgemuth-Ueberwasser, C.C., Hofmann, A., McKeegan, K.D., 2014. Coupled Fe and S isotope variations in pyrite nodules from Archean shale. Earth Planet. Sci. Lett. 392, 67–79.
- Marin-Carbonne, J., Busigny, V., Miot, J., Rollion-Bard, C., Muller, E., Drabon, N., Jacob, D., Pont, S., Robyr, M., Bontognali, T.R.R., François, C., Reynaud, S., Van Zuilen, M., Philippot, P., 2020. In Situ Fe and S isotope analyses in pyrite from the 3.2 Ga Mendon Formation (Barberton Greenstone Belt, South Africa): evidence for early microbial iron reduction. Geobiology 18, 306–325.
- Matthews, A., Morgans-Bell, H.S., Emmanuel, S., Jenkyns, H.C., Erel, Y., Halicz, L., 2004. Controls on iron-isotope fractionation in organic-rich sediments (Kimmeridge Clay, Upper Jurassic, Southern England). Geochim. Cosmochim. Acta 68, 3107–3123.
- Nabelek, P.I., 2020. Petrogenesis of leucogranites in collisional orogens. Geol. Soc. Lond. Spec. Publ. 491, 179–207.
- Nie, N.X., Dauphas, N., Alp, E.E., Zeng, H., Sio, C.K., Hu, J.Y., Chen, X., Aarons, S.M., Zhang, Z., Tian, H., Wang, D., Prissel, K.B., Greer, J., Bi, W., Hu, M.Y., Zhao, J., Shahar, A., Roskosz, M., Teng, F., Krawczynski, M.J., Heck, P.R., Spear, F.S., 2021. Iron, magnesium, and titanium isotopic fractionations between garnet, ilmenic fayalite, biotite, and tourmaline: results from NRIXS, ab initio, and study of mineral separates from the Moosilauke metapelite. Geochim. Cosmochim. Acta 302, 18–45.
- O'Neill, H.St.C., Berry, A.J., Mallmann, G., 2018. The oxidation state of iron in Mid-Ocean Ridge Basaltic (MORB) glasses: implications for their petrogenesis and oxygen fugacities. Earth Planet. Sci. Lett. 504, 152–162.
- Ostrander, C.M., Severmann, S., Gordon, G.W., Kendall, B., Lyons, T.W., Zheng, W., Roy, M., Anbar, A.D., 2022. Significance of 56Fe depletions in late-Archean shales and pyrite. Geochim. Cosmochim. Acta 316, 87–104.
- Patiño Douce, A.E., Beard, J.S., 1995. Dehydration-melting of Biotite Gneiss and Quartz Amphibolite from 3 to 15 kbar. J. Petrol. 36, 707–738.
- Patiño Douce, A.E., Harris, N., 1998. Experimental constraints on Himalayan Anatexis. J. Petrol. 39, 689–710.
- Planavsky, N., Rouxel, O.J., Bekker, A., Hofmann, A., Little, C.T.S., Lyons, T.W., 2012. Iron isotope composition of some Archean and Proterozoic iron formations. Geochim. Cosmochim. Acta 80, 158–169.
- Poitrasson, F., Freydier, R., 2005. Heavy iron isotope composition of granites determined by high resolution MC-ICP-MS. Chem. Geol. 222, 132–147.
- Polyakov, V.B., Clayton, R.N., Horita, J., Mineev, S.D., 2007. Equilibrium iron isotope fractionation factors of minerals: reevaluation from the data of nuclear inelastic resonant X-ray scattering and Mössbauer spectroscopy. Geochim. Cosmochim. Acta 71, 3833–3846.
- Richards, J.P., 2011. Magmatic to hydrothermal metal fluxes in convergent and collided margins. Ore Geol. Rev. 40, 1–26.
- Roskosz, M., Sio, C.K.I., Dauphas, N., Bi, W., Tissot, F.L.H., Hu, M.Y., Zhao, J., Alp, E.E., 2015. Spinel–olivine–pyroxene equilibrium iron isotopic fractionation and applications to natural peridotites. Geochim Cosmochim Acta 169, 184–199.
- applications to natural peridotites. Geochim. Cosmochim. Acta 169, 184–199.
  Roskosz, M., Dauphas, N., Hu, J., Hu, M.Y., Neuville, D.R., Brown, D., Bi, W., Nie, N.X., Zhao, J., Alp, E.E., 2022. Structural, redox and isotopic behaviors of iron in geological silicate glasses: A NRIXS study of Lamb-Mössbauer factors and force constants. Geochim. Cosmochim. Acta 321, 184–205.
- Rouxel, O.J., Bekker, A., Edwards, K.J., 2005. Iron isotope constraints on the Archean and Paleoproterozoic Ocean Redox State. Science 307, 1088–1091.
- Schauble, E.A., 2004. Applying stable isotope fractionation theory to new systems. Rev. Mineral. Geochem. 55, 65–111.
- Schuessler, J.A., Schoenberg, R., Sigmarsson, O., 2009. Iron and lithium isotope systematics of the Hekla volcano, Iceland — evidence for Fe isotope fractionation during magma differentiation. Chem. Geol. 258, 78–91.
- Simon, A.C., Pettke, T., Candela, P.A., Piccoli, P.M., Heinrich, C.A., 2004. Magnetite solubility and iron transport in magmatic-hydrothermal environments. Geochim. Cosmochim. Acta 68, 4905–4914.
- Slotznick, S.P., Eiler, J.M., Fischer, W.W., 2018. The effects of metamorphism on iron mineralogy and the iron speciation redox proxy. Geochim. Cosmochim. Acta 224, 96–115
- Sossi, P.A., Foden, J.D., Halverson, G.P., 2012. Redox-controlled iron isotope fractionation during magmatic differentiation: an example from the Red Hill intrusion, S. Tasmania. Contrib. Mineral. Petrol. 164, 757–772.
- Sossi, P.A., Nebel, O., Foden, J., 2016. Iron isotope systematics in planetary reservoirs. Earth Planet. Sci. Lett. 452, 295–308.
- Spear, F.S., 1993. Metamorphic phase equilibria and pressure-temperature-time paths. Mineral. Soc. Am. Monogr. 352–356.
- Spear, F.S., Kohn, M.J., Cheney, J.T., 1999. P-T paths from anatectic pelites. Contrib. Miner. Petrol. 134, 17–32.
- Stevens, G., Clemens, J., 1993. Fluid-absent melting and the roles of fluids in the lithosphere: a slanted summary? Chem. Geol. 108, 1–17.

- Sylvester, P.J., 1998. Post-collisional strongly peraluminous granites. Lithos 45, 29–44. Taylor, P.D.P., Maeck, R., be Bièvre, P., 1992. Determination of the absolute isotopic composition and Atomic Weight of a reference sample of natural iron. Int. J. Mass Spectrom. Ion Process. 121, 111–125.
- Telus, M., Dauphas, N., Moynier, F., Tissot, F.L.H., Teng, F.Z., Nabelek, P.I., Craddock, P. R., Groat, L.A., 2012. Iron, zinc, magnesium and uranium isotopic fractionation during continental crust differentiation: the tale from migmatites, granitoids, and pegmatites. Geochim. Cosmochim. Acta 97, 247–265.
- Teng, F.-Z., Dauphas, N., Huang, S., Marty, B., 2013. Iron isotopic systematics of oceanic basalts. Geochim. Cosmochim. Acta 107, 12–26.
- Terry, R.D., Chilingar, G.V., 1955. Summary of "Concerning some additional aids in studying sedimentary formations", by M. S. Shvetsov. J. Sediment. Res. 25, 229–234.
- Thompson, A.B., 1982. Dehydration melting of pelitic rocks and the generation of H<sub>2</sub>O-undersaturated granitic liquids. Am. J. Sci. 282, 1567–1595.
  Tomkins, A.G., 2010. Windows of metamorphic sulfur liberation in the crust:
- implications for gold deposit genesis. Geochim. Cosmochim. Acta 74, 3246–3259. Urey, H.C., 1947. The thermodynamic properties of isotopic substances. J. Chem. Soc. Resumed 562.
- Valley, J. W., 1986. Stable isotopes in high temperature geological processes. In: Valley, J.W., Taylor, H.P., O'Neil, J.R. (Eds.), De Gruyter, pp. 445–490.
- Wang, S.-J., Li, S.-G., Chen, L.-J., He, Y.-S., An, S.-C., Shen, J., 2013. Geochronology and geochemistry of leucosomes in the North Dabie Terrane, East China: implication for post-UHPM crustal melting during exhumation. Contrib. Miner. Petrol. 165, 1009–1029.
- Wang, Y., Zhu, X., Tang, C., Mao, J., Chang, Z., 2021. Discriminate between magmaticand magmatic-hydrothermal ore deposits using Fe isotopes. Ore Geol. Rev. 130, 103946.
- Warr, L.N., 2021. IMA–CNMNC approved mineral symbols. Mineral. Mag. 85, 291–320.
  Wawryk, C.M., Foden, J.D., 2015. Fe-isotope fractionation in magmatic-hydrothermal mineral deposits: a case study from the Renison Sn–W deposit, Tasmania. Geochim. Cosmochim. Acta 150, 285–298.
- White, R.W., Powell, R., Clarke, G.L., 2002. The interpretation of reaction textures in Ferich metapelitic granulites of the Musgrave Block, central Australia: constraints from mineral equilibria calculations in the system K<sub>2</sub>O-FeO-MgO-Al<sub>2</sub>O<sub>3</sub>-SiO<sub>2</sub>-H<sub>2</sub>O-TiO<sub>2</sub>-Fe<sub>2</sub>O<sub>3</sub>. J. Metam. Geol. 20, 41–55.
- White, R.W., Powell, R., Holland, T.J.B., Johnson, T.E., Green, E.C.R., 2014a. New mineral activity-composition relations for thermodynamic calculations in metapelitic systems. J. Metam. Geol. 32, 261–286.
- White, R.W., Powell, R., Johnson, T.E., 2014b. The effect of Mn on mineral stability in metapelites revisited: new a-x relations for manganese-bearing minerals. J. Metam. Geol. 32, 809–828.
- Whitehouse, M.J., Fedo, C.M., 2007. Microscale heterogeneity of Fe isotopes in >3.71 Ga banded iron formation from the Isua Greenstone Belt, southwest Greenland. Geology 35, 719–722
- White, Powell, Holland, Worley, 2000. The effect of TiO2 and Fe2O3 on metapelitic assemblages at greenschist and amphibolite facies conditions: mineral equilibria calculations in the system K<sub>2</sub>O–FeO–MgO–Al<sub>2</sub>O<sub>3</sub>–SiO<sub>2</sub>–H<sub>2</sub>O–TiO<sub>2</sub>–Fe<sub>2</sub>O<sub>3</sub>. J. Metam. Geol. 18, 497–511.
- Xu, L.-J., He, Y., Wang, S.-J., Wu, H., Li, S., 2017. Iron isotope fractionation during crustal anatexis: constraints from migmatites from the Dabie orogen, Central China. Lithos 284–285, 171–179.
- Yamaguchi, K.E., Johnson, C.M., Beard, B.L., Ohmoto, H., 2005. Biogeochemical cycling of iron in the Archean-Paleoproterozoic Earth: constraints from iron isotope variations in sedimentary rocks from the Kaapvaal and Pilbara Cratons. Chem. Geol. 218, 135–169.
- Yardley, B.W.D., 2005. Metal concentrations in crustal fluids and their relationship to ore formation. Econ. Geol. 100, 613–632.
- Yardley, B.W.D., 2013. The chemical composition of metasomatic fluids in the crust. In: Harlov, D.E., Austrheim, H. (Eds.), Metasomatism and the Chemical Transformation of Rock: The Role of Fluids in Terrestrial and Extraterrestrial Processes. Lecture Notes in Earth System Sciences. Springer, Berlin, Heidelberg, pp. 17–51.
- Yardley, B.W., Bodnar, R.J., 2014. Fluids in the continental crust. Geochem. Perspect. 3, 1–2.
- Yoshiya, K., Nishizawa, M., Sawaki, Y., Ueno, Y., Komiya, T., Yamada, K., Yoshida, N., Hirata, T., Wada, H., Maruyama, S., 2012. In situ iron isotope analyses of pyrite and organic carbon isotope ratios in the Fortescue Group: metabolic variations of a Late Archean ecosystem. Precambr. Res. 212–213, 169–193.
- Yoshiya, K., Sawaki, Y., Hirata, T., Maruyama, S., Komiya, T., 2015a. In-situ iron isotope analysis of pyrites in  $\sim$ 3.7 Ga sedimentary protoliths from the Isua supracrustal belt, southern West Greenland. Chem. Geol. 401, 126–139.
- Yoshiya, K., Sawaki, Y., Shibuya, T., Yamamoto, S., Komiya, T., Hirata, T., Maruyama, S., 2015b. In-situ iron isotope analyses of pyrites from 3.5 to 3.2 Ga sedimentary rocks of the Barberton Greenstone Belt, Kaapvaal Craton. Chem. Geol. 403, 58–73.
- Zajacz, Z., Halter, W.E., Pettke, T., Guillong, M., 2008. Determination of fluid/melt partition coefficients by LA-ICPMS analysis of co-existing fluid and silicate melt inclusions: controls on element partitioning. Geochim. Cosmochim. Acta 72, 2169–2197.
- Zhang, Z.J., Dauphas, N., Johnson, A.C., Aarons, S.M., Bennett, V.C., Nutman, A.P., MacLennan, S., Schoene, B., 2023. Titanium and iron isotopic records of granitoid crust production in diverse Archean cratons. Earth Planet. Sci. Lett. 620, 118342.